

This is the peer reviewed version of the following article: Wang, X., Yin, Z. Y., Xiong, H., Su, D., & Feng, Y. T. (2021). A spherical-harmonic-based approach to discrete element modeling of 3D irregular particles. *International Journal for Numerical Methods in Engineering*, 122(20), 5626-5655, which has been published in final form at <https://doi.org/10.1002/nme.6766>. This article may be used for non-commercial purposes in accordance with Wiley Terms and Conditions for Use of Self-Archived Versions. This article may not be enhanced, enriched or otherwise transformed into a derivative work, without express permission from Wiley or by statutory rights under applicable legislation. Copyright notices must not be removed, obscured or modified. The article must be linked to Wiley's version of record on Wiley Online Library and any embedding, framing or otherwise making available the article or pages thereof by third parties from platforms, services and websites other than Wiley Online Library must be prohibited.

A spherical-harmonic-based approach to discrete element modeling of 3D irregular particles

Xiang Wang, Zhen-Yu Yin, Hao Xiong*, Dong Su*, Y. T. Feng

Xiang WANG, Ph.D.

Postdoctoral Researcher, Department of Civil and Environmental Engineering, The Hong Kong Polytechnic University, Hong Kong, China; College of Civil and Transportation Engineering, Shenzhen University, Shenzhen, China. Email: xiang.wang@polyu.edu.hk; Phone: 86-15602988064

Zhen-Yu YIN, Ph.D.

Associate Professor, Department of Civil and Environmental Engineering, The Hong Kong Polytechnic University, Hong Kong, China. Email: zhenyu.yin@polyu.edu.hk

Hao XIONG, Ph.D. (Corresponding Author)

Assistant Research Professor, College of Civil and Transportation Engineering, Shenzhen University, Shenzhen, China. Email: xionghao19529@szu.edu.cn; Phone: 86-18923709898

Dong SU, Ph.D. (Corresponding Author)

Professor, College of Civil and Transportation Engineering, Shenzhen University, Shenzhen, China. Email: sudong@szu.edu.cn; Phone: 86-13823525942

Y. T. Feng, Ph.D.

Professor, Zienkiewicz Centre for Computational Engineering, College of Engineering, Swansea University, UK. Email: y.feng@swansea.ac.uk

A research article submitted to

International Journal for Numerical Methods in Engineering

First submission: December 2020

Abstract: Different from previous discrete element methods (DEM) where irregular 3D particle shapes are approximated by subspheres, vertices or voxels, this study aims to develop an innovative and computationally effective DEM method directly employing spherical harmonic functions for simulations of 3D irregular-shaped particles. First, the discrete surface points of a 3D irregular-shaped particle are represented by spherical harmonic functions with only a limited number of harmonic coefficients to restore the particle morphology. Then, the intrinsic physical quantities are computed directly using spherical harmonic functions. Next, specific algorithms for interparticle overlapping detection and contact resolution involving the spherical harmonic functions are developed. Subsequently, the interparticle contact forces, moments, and particle movements are computed. The feasibility and capability of the proposed 3D method is verified by simulating random deposition of superellipsoids, repose angle tests and triaxial tests on particles with various shapes. The proposed method could pave a viable pathway for realistic modeling of granular media pertaining to various engineering and industrial processes.

Keywords: Spherical harmonics; discrete element method; irregular shaped particles; micromechanics; contact detection and resolution

1 Introduction

Granular materials, such as sands, gravels and rock aggregates, comprise of particles with various irregular shapes that to a large extent determine the materials' complicated mechanical behaviors and properties [1]-[6]. Different DEM approaches were developed to consider various levels of particle shapes. For instance, for form-scale shape features, ellipses [7], ellipsoids [8][9], elongated particle models with rounded caps [10][11], and spherocylindrical particle models [12] were developed to consider the elongation effects of particles in DEM. Considering the roundness-scale shape features of realistic granular materials, superellipsoid [13], super-quadric [14], egg-shaped particles [15], polyellipsoid [16], and polysuperellipsoid [17] were developed to simulate symmetric and asymmetric shape particles with different corner sharpness. To capture the random irregularities of the granular particles, the polygon/polyhedron-based DEMs were developed by many researchers [18]-**Error! Reference source not found..** For instance, Feng and Tan [19] used Minkowski-difference to model convex polygon/polyhedron particles. Their proposed method was very effective and also energy-conserving. The Minkowski difference and GJK algorithms have also been implemented for convex polyhedrons in an open-source code SudoDEM [20]. However, these DEMs can hardly replicate the concave and convex surface morphologies of realistic irregular-shaped particles.

To simulate concave and convex irregular-shaped particles, the clump-based DEM was first developed based on the ODEC algorithm [21][22]. Although the clump method enables the investigation of particle-shape effects on various behaviour of particle systems [23][24], the

unrealistic multiple contacts between clump-based particles could result in unreasonable simulation results [25]-[27], e.g., over-stiff and over-damped responses. Moreover, some other alternative DEM programs to improve the weakness of clump-based DEM were also proposed, e.g., the granular element method (GEM) [28], the improved NURBS-based DEM [29], the LS-DEM [30]. Nevertheless, when dealing with particles with distinctive sizes and huge numbers, these methods would be computationally expensive.

To overcome the abovementioned problems, Lai et al. [31] first developed the FS-DEM to simulate 2D irregular-shaped particles. In the FS-DEM, the arbitrary 2D particle outlines can be continuously described using the Fourier series. However, their study was constrained in 2D plane. There are very limited studies on exploring the possibility of incorporating the harmonic series into DEM to simulate 3D irregular-shaped particles [2][6]. Furthermore, Feng et al. established a generic contact theory for arbitrary shaped particles [32]. Recently, more advanced algorithms were proposed by Feng [33][34] to ensure that the energy is conserved for elastic impact, leading to robust simulations of real problems involving arbitrarily shaped particles. Some successful implementations in both FDEM [35]-[38] and DEM [39][40] have also been conducted to resolve the explicit dynamics of irregular and real shape particles. Overall, it remains a challenge to model arbitrary shapes of realistic particles in DEM.

Accordingly, in this study, spherical harmonics, as a well-known higher-dimensional analogy of the Fourier-series, is employed to develop an innovative spherical harmonics-based discrete element method (SH-DEM) for simulating 3D irregular-shaped particles. First, the discrete surface points of a 3D irregular-shaped particle are represented by the spherical harmonic

function, where only a limited number of harmonic coefficients are required to restore the particle morphology. Then, the intrinsic physical quantities, which are necessary for computational mechanics, are computed directly using the spherical harmonic function. Next, specific algorithms for overlapping detection and contact resolution are developed for SH-based particles. Subsequently, the computation of the interparticle contact forces, moments, and particle movements is implemented. Finally, several numerical simulations are performed to illustrate the feasibility and capability of the proposed SH-DEM.

2 SH-based irregular-shaped particle model in DEM

2.1 Spherical-harmonic-transform of the particle surface

Several advanced techniques, such as X-ray tomography [1] and 3D laser scanning [6], have been employed to acquire the 3D surface information for realistic particles. Since the early 2000s, researchers have started to implement the acquisition and modelling of particle systems with real shapes [41]. As illustrated in Fig. 1 (a), the obtained 3D surface data is commonly in the format of triangular meshes, which is a typical discretized 3D surface model. As illustrated in Fig. 1 (b), the discrete vertices coordinate of the triangular mesh model determines the morphology of the irregular-shaped particle. In order to implement spherical harmonic transformation, the geometrical center of the particle is set as the origin of the spherical coordinate system and the coordination transformation process is performed to transform all the discrete vertices (x, y, z) of triangular meshes into spherical coordinates (θ, φ, r) . Once the spherical coordinates of a particle are obtained, the spherical harmonic function can then be

105 used to process the data. The spherical harmonic function is a well-known higher-dimensional
 106 analogy of Fourier series, defined on the surface of a sphere. Based on the spherical harmonic
 107 function, the surface coordinates $r(\theta, \varphi)$ of a particle can be expressed as the superimposition
 108 of a series of spherical harmonic basis functions:

$$r(\theta, \varphi) = \sum_{n=0}^N \sum_{m=-n}^n a_n^m Y_n^m(\theta, \varphi) \quad (1)$$

109 where N is the highest order number of the spherical harmonic basis functions; $\theta \in [0, \pi]$
 110 and $\varphi \in [0, 2\pi]$; $Y_n^m(\theta, \varphi)$ represents the harmonic basis function of order n and degree m ;
 111 a_n^m is the coefficient corresponding to $Y_n^m(\theta, \varphi)$. A group of N harmonics contains
 112 $(N + 1)^2$ number of a_n^m and $Y_n^m(\theta, \varphi)$. The basic function $Y_n^m(\theta, \varphi)$ is defined as:

$$Y_n^m(\theta, \varphi) = \sqrt{\frac{(2n + 1)(n - |m|)!}{4\pi(n + |m|)!}} P_n^m(\cos \theta) e^{im\varphi} \quad (2)$$

113 where $P_n^m(x)$ is the related Legendre polynomial:

$$P_n^m(x) = (-1)^{|m|} \cdot (1 - x^2)^{\frac{|m|}{2}} \cdot \frac{d^{|m|} P_n(x)}{dx^{|m|}} \quad (3)$$

114 in which $P_n(x)$ is the n^{th} order Legendre polynomial:

$$P_n(x) = \frac{1}{2^n n!} \frac{d^n [(x^2 - 1)^n]}{dx^n} \quad (4)$$

115 Assume that there are a total of N_p points on the particle surface. Substituting these N_p
 116 spherical coordinates $r(\theta, \varphi)$ into Eq. (4), we can obtain N_p linear equations:

$$\left\{ \begin{array}{l} r_1 = \sum_{n=0}^N \sum_{m=-n}^n a_n^m Y_n^m(\theta_1, \varphi_1) \\ \vdots \\ r_i = \sum_{n=0}^N \sum_{m=-n}^n a_n^m Y_n^m(\theta_i, \varphi_i) \\ \vdots \\ r_{N_P} = \sum_{n=0}^N \sum_{m=-n}^n a_n^m Y_n^m(\theta_{N_P}, \varphi_{N_P}) \end{array} \right. \quad (5)$$

117 In Eq. (5), $r_1 \sim r_{N_P}$ and $Y_n^m(\theta_1, \varphi_1) \sim Y_n^m(\theta_{N_P}, \varphi_{N_P})$ are all known while there are
 118 $(N + 1)^2$ unknown coefficients a_n^m . It is worth noting that, according to the previous studies
 119 [1], $N = 15$ is probably sufficient to represent the particle morphology. Since N_P can always
 120 be much larger than $(N + 1)^2$, it is easy to solve these coefficients with N_P equations through
 121 least-squares estimation.

122 2.2 Representation of particle surface by inverse SHT

123 After $(N + 1)^2$ harmonic coefficients are obtained for the discrete surface points of a target
 124 particle, as detailed in Section 2.1, we can use the $(N + 1)^2$ harmonic functions to represent
 125 the discretized surface points as a continuous closed surface. This process, namely the inverse
 126 operation of spherical harmonic transformation, is described as follows:

127 (1) Assume a random point $P_i(r_i, \theta_i, \varphi_i)$ with polar radius r_i and polar angle (θ_i, φ_i) is on
 128 the particle surface. When N_P surface points are required, N_P unit vertices
 129 $[(1, \theta_1, \varphi_1), \dots, (1, \theta_i, \varphi_i), \dots, (1, \theta_{N_P}, \varphi_{N_P})]$ uniformly surrounding the origin of the spherical
 130 coordinate system is determined based on the antipodal symmetry based scheme as adopted in

131 the our previous work [3]. These unit vertices can be regarded as a series of points equally
 132 distributed on a sphere. Then, based on the spherical harmonic function, compute the
 133 corresponding surface points $[(1, \theta_1, \varphi_1), \dots, (1, \theta_i, \varphi_i), \dots, (1, \theta_{N_p}, \varphi_{N_p})]$ on the particle. It
 134 should be noted that N_p needs to be sufficiently large if a high-quality 3D triangular mesh
 135 model is required.

136 (2) Substitute (θ_i, φ_i) into Eq. (3) to obtain the corresponding $Y_n^m(\theta_i, \varphi_i)$. For a certain
 137 harmonic order n , superimpose $(2n + 1)$ $a_n^m Y_n^m(\theta, \varphi)$ together, where m is the integer
 138 varying from $-n$ to n . Repeat this process from $n = 1$ to N , and superimpose them to obtain
 139 the final result of $r(\theta, \varphi)$.

140 (3) Finally, the coordinate transform can be used to obtain the Cartesian coordinates (x_i, y_i, z_i)
 141 of the particle surface. Fig. 1 (c) illustrated the reconstructed SH-based model. Since the above-
 142 detailed inverse SHT process can be used to calculate the coordinates of any surface points P_i ,
 143 the 3D irregular-shaped particle surface can thus be continuously represented by the spherical
 144 harmonic function.

145 **2.3 Intrinsic physical quantities of SH-based particle**

146 The intrinsic physical quantities, such as the mass and moment of inertia, for each SH-based
 147 particle, can be directly calculated from the adopted spherical harmonic functions that are used
 148 to generate the corresponding particle.

149 (1) Mass of a 3D irregular-shaped particle

150 The mass of a 3D irregular-shaped particle with uniform density ρ can be computed by:

$$m = \rho \cdot V \quad (6)$$

151 where V is the volume of the SH-based particle. In the proposed SH-DEM approach, the

152 volume of the particle can be calculated by integrating the radical distance r over the spherical

153 angles θ, φ :

$$V = \frac{1}{3} \int_0^\pi \int_0^{2\pi} r(\theta, \varphi)^3 \sin(\theta) d\varphi d\theta \quad (7)$$

154 where the radical distance r at any spherical angle pair (θ, φ) can be obtained using the

155 spherical harmonic function, as given in Eq. (1).

156 (2) Moment of inertia

157 For an SH-based particle, the moment of inertia around three Cartesian coordinate axes can be

158 expressed as a tensor \mathbf{I} :

$$\mathbf{I} = \begin{bmatrix} I_{xx} & -I_{xy} & -I_{xz} \\ -I_{xy} & I_{yy} & -I_{yz} \\ -I_{xz} & -I_{yz} & I_{zz} \end{bmatrix} \quad (8)$$

159 where I_{xx} , I_{xy} , I_{yz} , I_{yy} , I_{xz} and I_{zz} can be calculated by:

$$I_{xx} = \frac{1}{5} \rho \int_0^\pi \int_0^{2\pi} r(\theta, \varphi)^5 \sin(\theta) ((\sin(\theta) \sin(\varphi))^2 + (\cos(\theta))^2) d\varphi d\theta \quad (9)$$

$$I_{yy} = \frac{1}{5} \rho \int_0^\pi \int_0^{2\pi} r(\theta, \varphi)^5 \sin(\theta) ((\sin(\theta) \cos(\varphi))^2 + (\cos(\theta))^2) d\varphi d\theta$$

$$I_{zz} = \frac{1}{5} \rho \int_0^\pi \int_0^{2\pi} r(\theta, \varphi)^5 \sin(\theta)^3 d\varphi d\theta$$

$$I_{xy} = \frac{1}{5} \rho \int_0^\pi \int_0^{2\pi} r(\theta, \varphi)^5 \sin(\theta)^3 \cos(\varphi) \sin(\varphi) d\varphi d\theta$$

$$I_{xz} = \frac{1}{5} \rho \int_0^\pi \int_0^{2\pi} r(\theta, \varphi)^5 \sin(\theta)^2 \cos(\theta) \cos(\varphi) d\varphi d\theta$$

$$I_{yz} = \frac{1}{5} \rho \int_0^\pi \int_0^{2\pi} r(\theta, \varphi)^5 \sin(\theta)^2 \cos(\theta) \sin(\varphi) d\varphi d\theta$$

160 It is worth noting that, the tensor \mathbf{I} needs to be computed first based on a coordinate system
 161 (whatever it is), then the principal moment axes are obtained to form a local coordinate system.
 162 Finally, the SH-based particles will always be rotated at the local frame where each principal
 163 moment of inertia is along one coordinate axis.

164 **3 Computation of interactions between SH-based particles**

165 In this section, we develop unique algorithms for overlapping detection and contact resolution
 166 of SH-based particles. First, the spherical harmonic function is combined with the node-to-
 167 surface approach to examine the overlapping condition between two collision candidate
 168 particles. Second, the contact point and contact normal vector of each penetration node can be
 169 quickly calculated based on the proposed scheme in the SH-DEM. Third, the normal contact
 170 force is computed for each penetration node based on the volumetric normal contact stiffness
 171 and local overlapping volume.

3.1 Overlapping detection for 3D irregular-shaped particle

(1) Global overlapping detection

In the first stage, irregular-shaped particles are circumscribed by the axis-aligned bounding boxes (AABBs). The boundaries ($X_{min}, X_{max}, Y_{min}, Y_{max}, Z_{min}, Z_{max}$) of the AABB for a 3D irregular-shaped particle are illustrated in Fig. 2. Then, the modeling domain is divided into $N_{bx} \times N_{by} \times N_{bz}$ cubic bins. Next, the obtained AABBs are entered into cells (i.e., spatial bins) in the cell space based on an enlarged extent (i.e., cell extent). Once the cell extents of two particles overlap, the two particles are considered as a collision candidate. More specifically, if a particle shares at least one single cell bin with one of its neighbors, further detection is required to examine the potential collision between them.

(2) Local overlapping detection

The spherical harmonic function is combined with the node-to-surface approach to examine the local overlapping condition if two neighboring particles are detected as potentially overlapped using the global overlapping detection algorithm. The node-to-surface scheme has previously been employed in finite element methods [42][43] as well as discrete element methods [30][44] to deal with the contact problems between irregular-shaped particles where the contact interface is non-convex shape and multiple contact points may exist. The detailed procedure for the local overlapping detection is as follows:

Step 1: If two neighboring particles are detected as potentially overlapping at the global overlapping detection stage, select the particle with a smaller volume as a Master Grain (MG),

192 while the other is regarded as the Slave Grain (SG). Then, as illustrated in Fig. 3, under the local
193 spherical coordination system of the MG (in blue), determine the potential overlapping range
194 (in red) of spherical angles where the circumscribed spheres of the two particles intersect.

195 Step 2: As illustrated in Fig. 4, the SG is represented by the spherical harmonic function
196 $r^S(\theta, \varphi)$, while the particle surface of the MG in the potential overlapping range is discretized
197 into triangular meshes with a certain number of vertices $Q_i[r_i^M(\theta_i, \varphi_i)]$, which are seeded on
198 the particle surface at a uniform interval based on the antipodal symmetry based scheme as
199 adopted in our previous work [3]. It is worth noting that the density of the discretized nodes on
200 the MG can be quantitatively controlled and easily increased if more accurate modeling
201 resolution is required.

202 Step 3: Transform each of the discretized vertices on the MG from its local coordinate system
203 into the local spherical coordinate system of the SG, $Q_i[r_i^M(\theta_i, \varphi_i)]$. Then, as illustrated in Fig.
204 5, the overlapping condition is determined by checking each $Q_i[r_i^M(\theta_i, \varphi_i)]$ against the SH-
205 based surface function $r^S(\theta, \varphi)$ of the SG for penetration. If $Q_i[r_i^M(\theta_i, \varphi_i)] > r^S(\theta_i, \varphi_i)$, the
206 vertex $Q_i[r_i^M(\theta_i, \varphi_i)]$ is outside the surface of the SG. If $Q_i[r_i^M(\theta_i, \varphi_i)] = r^S(\theta_i, \varphi_i)$,
207 $Q_i[r_i^M(\theta_i, \varphi_i)]$ lies on the surface of the SG. If $r_i^M(\theta_i, \varphi_i) < r^S(\theta_i, \varphi_i)$, vertex
208 $Q_i[r_i^M(\theta_i, \varphi_i)]$ penetrates the boundary of the SG. If any of the node Q_i is detected to
209 penetrate the SG, the overlap between MG and SG is then identified. It is noted that the density
210 of the discretized vertices on the potential overlapping region of the MG will not influence the
211 underlying surface morphology of the original particle, which is represented by its spherical
212 harmonic function, but the accuracy and computational cost will be affected.

213 3.2 Contact resolution for 3D irregular-shaped particle

214 As mentioned in the previous subsection, if overlapping is identified, the penetrating vertices
 215 $Q_i[r_i^M(\theta_i, \varphi_i)]$ of MG with $r_i^M(\theta_i, \varphi_i) < r^S(\theta_i, \varphi_i)$ can be extracted for the computation of
 216 contact points and inter-particle forces. For each penetrating vertex $Q_i[r_i^M(\theta_i, \varphi_i)]$ of the MG
 217 inside the SG, there is a corresponding vertex $P_i[r^S(\theta_i, \varphi_i)]$ on the SG by directly substituting
 218 (θ_i, φ_i) into the spherical harmonic function of $r^S(\theta, \varphi)$ of SG. For each pair of vertices Q_i
 219 and P_i , the contact point C_i , contact normal vector \vec{n}_i , and local overlapping volume V_i can
 220 be defined as follows:

221 (1) Contact point C_i

222 As illustrated in Fig. 6, the midpoint of the penetration points Q_i and P_i is defined as the
 223 contact point C_i for the local overlapping region of Q_iP_i , i.e., $C_i = (Q_i + P_i)/2$.

224 (2) Contact normal vector \vec{n}_i

225 As illustrated in Fig. 7, the sum of the outward normal vector \vec{n}_i^Q at vertex Q_i on the surface
 226 of MG and the inward normal vector \vec{n}_i^P at P_i on the surface of SG are computed to define
 227 the contact normal vector \vec{n}_i :

$$\vec{n}_i = \frac{\vec{n}_i^Q + \vec{n}_i^P}{\|\vec{n}_i^Q + \vec{n}_i^P\|} \quad (10)$$

228 where \vec{n}_i^Q is the inward normal vector at vertex Q_i on the MG, and \vec{n}_i^P is the outward normal
 229 vector at vertex P_i on the SG.

230 The contact normal vector is simple and easy to compute due to the formulation of the spherical
 231 harmonic function, whose outward normal vector at any spherical angle (θ, φ) can be easily
 232 obtained by:

$$\vec{n}(\theta, \varphi) = \left(-\frac{\partial \vec{R}(\theta, \varphi)}{\partial \theta} \times \frac{\partial \vec{R}(\theta, \varphi)}{\partial \varphi} \right) \quad (11)$$

233 where $\vec{R}(\theta, \varphi)$ is the position vector of the vertex, which is represented in the Cartesian
 234 coordinate system as:

$$\vec{R}(\theta, \varphi) = [r(\theta, \varphi) \cos \theta \cos \varphi, \quad r(\theta, \varphi) \cos \theta \sin \varphi, \quad r(\theta, \varphi) \sin \theta] \quad (12)$$

235 (3) Local overlapping volume V_i

236 As illustrated in Fig. 8, the local overlapping volume V_i can be computed by:

$$V_i = \frac{1}{3} \sum V_{P_i P_i^k P_i^{k+1} Q_i Q_i^k Q_i^{k+1}} \quad (13)$$

237 where (Q_i^k, Q_i^{k+1}) is the k^{th} pair of the one-ring neighboring vertex of Q_i on the MG, the
 238 definition of one-ring neighboring vertex has been detailed in our previous work [5];
 239 (P_i^k, P_i^{k+1}) are the vertices on the SG that correspond to (Q_i^k, Q_i^{k+1}) , which can be obtained
 240 by directly substituting $(\theta_i^k, \varphi_i^k)$ and $(\theta_i^{k+1}, \varphi_i^{k+1})$ into the spherical harmonic function of
 241 $r^S(\theta, \varphi)$ of SG. As shown in Fig. 8 (d), $V_{P_i P_i^k P_i^{k+1} Q_i Q_i^k Q_i^{k+1}}$ is the volume of the polyhedron
 242 formed by the six vertices. As shown in Fig. 8 (e), the local overlapping volume V_i is formed
 243 by Q_i , P_i , and the midpoints between their one-ring neighboring vertices.

3.3 Force and moment for 3D irregular-shaped particle

Different from the existing clump-based [21] and polyhedral-based [20] DEM, in the proposed SH-DEM, the contact forces between the identified neighboring particles are computed based on the defined contact point, normal contact direction, and local overlapping volume at each penetration node. The volume-based contact model is employed in the proposed SH-DEM to compute the normal contact force. It is worth noting that, as suggested by Feng [32]-[34], the conventional volume-based contact models may have a problem of energy increase for an elastic impact and thus becomes a source of potentially numerical instability. Thus, the energy-conserving contact theory [32]-[34] will be incorporated into the SHDEM in the future work to enhance the reliability and accuracy of the simulation.

The normal contact force at the contact point Q'_i resulting from the corresponding SG to MG is formulated as:

$$\vec{F}_{n,i}^M = k_n V'_i \vec{n}'_i \quad (14)$$

where k_n is the volumetric normal contact stiffness. If the material properties of the two touching irregular-shaped particles are different, k_n can be determined by:

$$k_n = \frac{k_n^M k_n^S}{k_n^M + k_n^S} \quad (15)$$

where the superscripts M and S denote the master grain and slave grain in contact.

By action and reaction, the resulting normal contact force at the contact point C'_i from the corresponding MG to SG can be computed as:

$$\vec{F}_{n,i}^S = -\vec{F}_{n,i}^M \quad (16)$$

261 Similar to other existing DEM algorithms, the tangential contact force is determined by the
 262 Coulomb friction model. To calculate the resultant tangential contact force $\vec{F}_{t,i}^M$ at the contact
 263 point C'_i from SG to MG, the relative velocity \vec{v}_i^M of C'_i to the SG is:

$$\vec{v}_i^M = \vec{v}^M + \omega^M \times (C'_i - c^M) - \vec{v}^S - \omega^S \times (C'_i - c^S) \quad (17)$$

264 where \vec{v}^M and ω^M are the translational and angular velocities of the MG, \vec{v}^S and ω^S are
 265 the translational and angular velocities of the SG, c^M and c^S are the mass centers of the MG
 266 and SG, respectively.

267 Then, the incremental tangential displacement Δu of the MG at the contact point C'_i relative
 268 to the SG is:

$$\Delta u = [\vec{v}_i^M - (\vec{v}_i^M \vec{n}'_i) \vec{n}'_i] \Delta t \quad (18)$$

269 Next, the tangential force from the SG on the MG at the contact point C'_i after Δt is updated
 270 as:

$$\vec{F}_{t,i}^M = \frac{\vec{Z} \vec{F}_{t,i}^{M'}}{\|\vec{Z} \vec{F}_{t,i}^{M'}\|} \min \left\{ \left\| \vec{Z} \vec{F}_{t,i}^{M'} - k_t \Delta u \right\|, \mu \|\vec{F}_{n,i}^M\| \right\} \quad (19)$$

271 where Z is the rotation matrix that rotates the normal vector \vec{n}'_i at the current time step to the
 272 normal vector at the previous time step, k_t is the tangential contact stiffness, and μ is the
 273 inter-particle friction coefficient. The occurrence of slide events at the contact is determined by
 274 the sliding friction model. If $\left\| \vec{Z} \vec{F}_{t,i}^{MS'} - k_t \Delta u \right\|$ is greater than $\mu \|\vec{F}_{n,i}^{MS}\|$, the slide event occurs

275 at the contact and $\vec{F}_{t,i}^{MS}$ is reduced to $\mu \|\vec{F}_{n,i}^{MS}\|$.

276 By action and reaction, the tangential force from MG on SG at the contact point C'_i is

$$\vec{F}_{t,i}^S = -\vec{F}_{t,i}^M \quad (20)$$

277 The moment \vec{M}_i^M contributed by the normal and tangential contact force $\vec{F}_{n,i}^M$, $\vec{F}_{t,i}^M$ at the
 278 contact point CP_i^M , resulting from the SG to the MG, is formulated by:

$$\vec{M}_i^M = (\vec{C}'_i - \vec{c}^M) \times (\vec{F}_{t,i}^M + \vec{F}_{n,i}^M) \quad (21)$$

279 Similarly, the moment \vec{M}_i^S contributed by the normal and tangential contact force $\vec{F}_{n,i}^S$, $\vec{F}_{s,i}^S$
 280 at the contact point C'_i , resulting from the MG to the SG, is formulated by:

$$\vec{M}_i^S = (\vec{C}'_i - \vec{c}^S) \times (\vec{F}_{t,i}^S + \vec{F}_{n,i}^S) \quad (22)$$

281 3.4 Particle kinematics and computational scheme

282 To simulate the kinematics of a large number of 3D irregular-shaped particles, the explicit time
 283 step approach is employed to compute the motion of the SH-based particles. The law of force-
 284 displacement (constitutive contact law) and the law of motion (Newton's second law) are used
 285 to calculate the contact force between particles and the movement of each particle at each time
 286 step, respectively. The computation of particle kinematics in the SH-DEM is detailed in
 287 Appendix A.

288 It is important to note that, to minimize the computational cost, the spherical harmonic function
 289 and corresponding discretized vertices of each SH-based particle are never updated as the

particle moves; each spherical harmonic function remains in a reference configuration. To accommodate this constraint, when computing the contact, the discretized nodes of the MG are first transformed temporarily from its local spherical coordinate system into the global Cartesian coordinate frame and are subsequently transformed temporarily into the reference configuration of the SG. In the local spherical coordinate system of the SG, the contact forces and moments are computed and then transformed back to the global coordinate system.

The whole computation procedure for irregular-shaped particle kinematics in the SH-DEM, which follows conventional DEM codes, is detailed in Appendix B. The proposed SH-DEM exhibits great efficiency in updating the irregular particle information at each time-step. Since each particle is represented by the spherical harmonic function, it only requires a few variables (i.e., the position of the particle center and the rotation angle of the local particle coordinate with reference to the global specimen coordinate) to restore the irregular 3D particle shapes. The harmonic coefficients remain constant and are independent of the particle motion and kinematics.

4 Numerical examples

4.1 Random packing of superellipsoid particles

Simulating the random packing of aspherical particles, e.g., superellipsoids, has been a hot issue among granular researchers [13][50][51] for many years. Through various laboratory experiments and numerical simulations, it has been revealed by many researchers that elongation and flatness play a significant role in both packing density and microscopic

310 structures of super-ellipsoid particles. Therefore, before simulating realistic irregular-shaped
 311 particles, we first focus on the random packing of ellipsoid particles to examine the consistency
 312 of SH-DEM simulations with existing studies. In this section, we focus on a typical type of
 313 super-ellipsoid particles with various form and blockiness shapes, which are determined by the
 314 shape control parameters η and ζ :

$$\left| \frac{x}{\eta c} \right|^{\frac{2}{\zeta}} + \left| \frac{y}{\eta c} \right|^{\frac{2}{\zeta}} + \left| \frac{z}{c} \right|^{\frac{2}{\zeta}} = 1 \quad (23)$$

315 where η determines the form shape, ζ determines the blockiness shape, and c determines
 316 the particle size. The adopted shapes generated by Eq. (23) are all special cases of super-
 317 quadrics [50][51].

318 In this section, we aim to reproduce the packing features of superellipsoid particles with η
 319 varying from 0.4 to 2.5 while ζ varying from 0.5 to 1.5. To ensure that the simulated packing
 320 features are only affected by the shape, the other particle properties are set to the same values
 321 for all simulation scenarios. The particle size r , defined as the radius of the sphere with
 322 equivalent volume) for each particle, is set as 10mm. The DEM simulation parameters are listed
 323 in Table 1, which are typical values for the simulation of rock aggregates in previous works
 324 [13][45]. To balance the modeling accuracy and the computational cost, N is set to 20 and N_p
 325 is set to 8000.

326 The gravitational layer-by-layer deposition approach is employed to simulate the random
 327 packing of superellipsoid particles. Each sample consists of 1200 non-overlapping particles,

i.e., 12 layers of 100 particles are sequentially added to a box. The box used to contain the particles is 100 mm in width and 100 mm in length. The height is set to 150 mm to facilitate enough space to allocate each layer of non-overlapping particles above existing particles. For each layer, 100 particles of 10 mm in diameters with random locations and orientations are distributed without overlapping in the box. When the existing particles reach an assumed equilibrium state, the next layer of particles is added sequentially. Fig. 9 shows some final packings for an initial observational comparison.

In the present study, two groups of particle shapes controlled by 12 values of η (Group A) and 12 values of ζ (Group B) are simulated to examine the macroscopic property - packing density. The simulation results are detailed as follows:

The packing density ρ of a granular particle assembly can be calculated as the volumetric percentage of the solid particles versus the total volume of the particle assembly, including particles and voids. As shown in Fig. 10 (a), for group A, the evolution of packing density versus increasing value of η for superellipsoid particles with $\zeta = 1$ are plotted and compared with the existing studies [13][46][47]. It can be seen in the figure that the trend is consistent with the results of other simulation studies in the previous literature. In general, all studies show two peak values of packing density. The first peak value of packing density exists when η is approximately 0.6, and the second peak value of packing density can be observed when η reaches approximately 1.5. This evolution trend of packing density versus η can be described as an “M” shaped relationship. This “M” shaped relationship between packing density and η is obviously observed in both the present and existing simulations. As shown in Fig.10 (b), for

group B, the evolution of packing density versus increasing value of ζ for superellipsoid particles with $\eta = 1$ are plotted and compared with the existing studies [13][48][49]. It is observed that there is a valley in the ζ - ρ curve, i.e., the particles with $\zeta = 1$ exhibit the lowest packing density. When ζ increases from 0.3 to 1.0, the packing density shows a negative relationship with ζ . When ζ further increases to be larger than 1.0, the packing density becomes positively related to ζ . This “V” shaped trend was also reported in previous simulations [13][48][49].

4.2 Repose angle tests of real crushed rock aggregates

The repose angle is a well-acknowledged physical property that has been employed by many researchers to calibrate the inter-particle friction coefficient of granular materials needed for DEM analysis. In this study, laboratory experiments for measuring the repose angle of crushed rocks are conducted, and the results are used to verify the validity of the developed SH-DEM program. The repose angle tests are conducted inside a container with glass sidewalls and a stone base, whose dimensions are 10 cm in width, 40 cm in length, and 20 cm in height, as shown in Fig. 11 (a). The crushed rocks are granite, with average aggregate sizes of 20 mm in diameter. In the test, approximately 300 crushed rocks are poured into the right part of the container, which is supported by a sidewall (baffle) at right, as shown in Fig. 11 (b). The dimensions of the rock assembly are kept as 10 cm in width, 10 cm in length, and 20 cm in height. Then, to ensure an optimal spreading of the material, the sidewall is lifted using a small velocity, as shown in Fig. 11 (c). During wall lifting, the crushed rocks collapse, roll and form a slope under gravity. Finally, after the collapsed crushed rocks stabilized, the repose angle is

measured using an angular ruler, as illustrated in Fig. 11 (*d*). The tests are repeated 20 times, and the experimental results reveal that the tested crushed rocks have an average repose angle of approximately 38.9° .

A numerical analysis of the angle of repose is performed using the proposed SH-DEM. As shown in Fig. 12, the real crushed rocks are first scanned using the 3D laser scanner, and the surface cloud points are imported into the SH-DEM to obtain realistic SH-based rock aggregates. The simulation process follows the same sequence as the laboratory experiment. First, the initial numerical samples for testing are prepared by sequentially adding the randomly selected SH-based real rocks into the right-side container, which consists of four virtual sidewalls in the DEM. At this stage, contact frictions are all set to 0.0 to guarantee a relatively dense packing condition. Other DEM simulation parameters follow previous studies, as listed in Table 1. As shown in Fig. 13 (*a*), the dimension of the initial sample is the same as the real case. During the simulation, the contact friction coefficient between rocks (aggregate to aggregate and aggregate to base-wall) is set to a specific value, and then the simulated baffle (in red) is slowly lifted, as shown in Fig. 13 (*b*). For each value of the contact friction coefficient, the tests are repeated 20 times to compute a mean repose angle, and the contact friction coefficient is incrementally changed to bring the simulated mean repose angle close to the average laboratory-measured value. Fig. 14 illustrates the repose angles of the samples with different contact friction coefficients. The results indicate that the contact friction coefficient should be taken as approximately 0.3 to simulate the realistic repose angle of crushed rocks.

The macroscopic and microscopic properties of rock aggregate assemblies are of great

importance to assessing engineering behaviors of the geo-body and the construction-body, e.g., slope, foundation, embankment, etc. Many researchers have reported that there are many factors, e.g., confining pressure, initial void ratio, and aggregate shape can significantly influence on the macro- and micromechanical properties of crushed rocks. In this section, we aim to examine the shape effects on the macro- and micromechanical properties of the rock assemblies during repose angle tests. Three simulations were conducted with crushed rock aggregates of various shapes. Fig. 15 shows the ranges of shapes and the snapshots of example aggregates, where sample S1 consists of spherical aggregates with $AR=1.0$, sample S2 consists of ellipsoidal aggregates with $AR=0.65$, and Sample S3 consists of real crushed rocks with mean $AR=0.65$. In the simulation, the material properties are consistent with the previous section, while the contact friction between rocks is kept as 0.3 during the baffle lifting and rock collapsing stages. The simulation results are detailed as follows:

(1) Fig. 16 illustrates the measured repose angles for each sample. It can be seen from the results that the spherical aggregates have the smallest repose angle (15°), the ellipsoid aggregates have an intermediate repose angle (28°), and the real crushed rock aggregates have the largest repose angle (37°). This trend occurs because more elongated and more irregular-shaped aggregates tend to have more considerable rolling resistance.

(2) The mean coordination number, Z , is a scalar parameter that provides macroscopic information on the internal structural features (fabric) of granular materials. The evolution of Z during baffle lifting and rock collapsing for all assemblies is illustrated in Fig. 17. In all cases, Z exhibits a gradual drop versus the increasing simulation time during the aggregate collapsing

stage. When the aggregates form a stable heap, Z slightly increases and then reaches a stable value. Among the three samples, sample S3 (with real crushed rocks) always exhibits larger values of Z during the whole testing period, compared with S1 (with smallest Z) and S2 (with intermediate Z). The results for Z reveal that more irregular-shaped aggregates tend to have denser packing structures during the test. Besides, S1 (spherical aggregates) shows an earlier drop at the initial stage, while the samples with more irregular aggregate shapes show more delayed decreasing trends.

(3) The rotation motions are governed by the rolling resistance of the aggregates. In the simulated repose angle tests, the rotational movements of the aggregates during collapsing mostly occur around the x -axis. Thus, the mean accumulated rotational displacement around the x -axis, ϑ_x , is computed. The results, as shown in Fig. 18, display the evolution of ϑ_x versus simulation times for different samples. In general, for all numerical cases, the ϑ_x values increase during the repose angle tests. For sample S1, the ϑ_x of spherical aggregates rises sharply and gradually converges to a stable value. For samples S2 and S3, the ϑ_x of ellipsoid and crushed rocks increase gradually and converge to a relatively small amount. It can be seen in the figure that aggregate shapes play a significant role in the rotational movements. During the whole process of the repose angle test, the spherical aggregates ($AR=1.0$) always exhibit a significantly larger ϑ_x , at approximately 5 times the value for the ellipsoids ($AR=0.65$) and 7 times the value for the crushed rocks ($AR=0.65$).

4.3 Triaxial shear tests of real crushed rock aggregates

The macroscopic and microscopic properties of rock particle assemblies are of great importance to the engineering behaviors of the geo-body and the construction-body, e.g., slope, foundation, embankment, etc. Many researchers have reported that there are many factors, such as confining pressure, initial void ratio, and particle shape, that can significantly influence on the macro- and micromechanical properties of crushed rocks. In this section, three simulation groups of triaxial shear tests on realistic crushed rocks are performed to numerically examine the effect of confining pressure, preshear void ratio, and particle shapes. Group A consists of three samples with confining pressures of 50 kPa, 100 kPa, and 200 kPa, respectively. Group B consists of three samples with various initial void ratios prepared by preshear contact friction of 0.00, 0.15, and 0.30. Group C consists of three samples with various mean aspect ratios ($\overline{AR} = 0.95, 0.80, 0.65$). Fig. 19 shows the ranges of shapes and snapshots of crushed rock examples in Group C. The procedure to conduct a triaxial shear test in the SH-DEM is summarized as follows:

(1) For the random allocation of non-overlapped particles, the particle models of crushed rocks in the “STL” file format are first imported into the spherical harmonic transformation subroutine of the present SH-DEM program to obtain the harmonic coefficients for each particle. Then, as shown in Fig. 20 (a), nonoverlapping particles are allocated into a prescribed sample domain, which is a cubic container consisting of six rigid walls. Each sample consisted of approximately 1500 particles of monodispersed sizes ($d_{ave} = 20 \text{ mm}$).

(2) In the stage of isotropic compression, before activating external force to the assembly, the properties of the material are assigned to all particles and walls to facilitate dynamic modeling in the SH-DEM. The input parameters are consistent with those used in the former section for real crushed rocks, except the wall friction ($\mu_{wall}=0$ and $\mu_{particle}=0.5$) and the preshear contact friction between particles ($\mu_{preshear}=0$ for Groups A and C, $\mu_{preshear}=0, 0.15, 0.30$ for Group B). The gravitational force is set as zero during the simulation. Then, the consolidation procedure is performed with the given confining stress to enable the assembly to reach an isotropic stress state. The stress-control wall servo scheme is employed to move the six rigid walls to maintain constant confining pressure, which shows an example of the preshear numerical samples of crushed rocks in the SH-DEM. Fig. 20 (b) shows an example of the preshear numerical sample of crushed rocks in the SH-DEM.

(3) During the triaxial shear stage, both the top and bottom walls move toward each other at a constant strain rate, while the four lateral sidewalls move individually to maintain a constant confining stress with the stress-control servo. The shear strain rate is set sufficiently low to obtain quasi-static behavior during shearing. Fig. 20 (c) shows an example of a numerical rock aggregate sample at shear strain of 50% in the SH-DEM.

In the present simulation, both macroscopic properties, e.g., deviatoric stress q , volumetric strain ε_v , and microscopic quantities, e.g., mean coordination number, and percentage of sliding contact are calculated at different axial strains ε_a . The results are detailed and discussed as follows:

(1) The deviatoric stress q is computed to study the shear strength of the assemblies.

Fig. 21 shows the deviatoric stress q as a function of axial strain ε_a for all specimens with different AR, preshear contact friction, and confining pressure. For specimens with different AR, all curves behave in a similar fashion, showing peak stress, i.e., the stress softening. AR tends to have a greater influence on postpeak behaviors. For peak state, the sample with AR=0.8 has the highest deviatoric stress, while in the residual state, the deviatoric stress increases with the smaller value of AR. For specimens with different preshear contact friction, the smaller value of PF leads to stress softening, while a larger value of PF leads to stress hardening. For the peak state, the deviatoric stress increases with decreasing PF, while in the residual state, PF shows a negligible influence on the deviatoric stress. For specimens with different confining pressures, all curves show significant peak deviatoric shear stress.

(2) The volumetric changes of different specimens during shearing are investigated. Given that the present cubic samples are bounded by rigid walls, the axial strain ε_1 and the volumetric strain ε_v can be approximately calculated based on the displacement of the boundary walls. As shown in Fig. 22, for groups A and C, the volumetric strain increases with increasing axial strain, and the specimens deform at constant volume after reaching the critical state at an axial strain ranging from 40% to 50%, which indicates that all specimens display shear-induced dilatancy behavior with stress softening. For Group B, according to the difference between the volumetric strain at the initial and residual states, the total volume change during shearing appears to increase as PF decreases, indicating that an assembly with a smaller preshear contact friction shows higher dilatancy during shearing.

(3) The coordination number is a scalar parameter that provides macroscopic information on the internal structural features (fabric) of granular materials. The mean coordination numbers of all samples, Z , are computed and compared. The evolution of Z against axial strain for all assemblies is illustrated in Fig. 23. In all cases, Z exhibits an exponential drop versus the increasing axial strain during the initial shearing process. When the axial strain is larger than 10%, Z reaches a low plateau with small fluctuations.

For Group A, the values of Z are always positively related to AR during the whole shear process, i.e., Z increases from 7 to 8 at the initial state and shifts from 4.3 to 5.7 at the residual state when AR varies from 0.65 to 0.95. For Group B, Z is only negatively related to PF during the initial shear process. At the initial state, Z increases from 5.3 to 7.2 when PF decreases from 0.3 to 0.0. When shear strain is larger than 10%, all samples with different PF show the same values of Z and converge to a constant value of about 4.7. As for Group C, similar to Group A, the values of Z are always positively related to the CP during the whole shear process. The values of Z vary from 7.1 to 7.6 at the initial state and shift from 4.2 to 4.9 at residual state when CP increases from 50 kPa to 200 kPa.

Besides, the sliding contacts are governed by Coulomb's friction law. We can denote the sliding ratio (R_{sc}) using the ratio between shear force f_t and normal force f_n at each contact:

$$R_{sc} = |f_t|/(\mu_c f_n) \quad (24)$$

We assumed that sliding event occurs at contact when $R_{sc} > 0.99$. Then, the percentage of sliding contact P_{sc} can be defined as:

$$P_{sc} = \frac{\sum_{i=1}^{N_c} G(R_{sc})}{N_c} \quad (25)$$

$$G(R_{sc}) = \begin{cases} 0 & R_{sc} \leq 0.99 \\ 1 & R_{sc} > 0.99 \end{cases}$$

511 where N_c is the total number of contacts.

512 Fig. 24 displays the evolution of P_{sc} versus axial strain ε_a . In general, for all numerical cases,
 513 P_{sc} increases sharply to a peak value, and then gradually decreases to a steady state.
 514 Additionally, for Group A, P_{sc} increases from 59% to 70% at the peak state, and increases
 515 from 40% to 47% at the steady state, when AR increases from 0.65 to 0.95. For Group B, the
 516 samples only show negative relationships between peak P_{sc} and PF , i.e., P_{sc} increases from
 517 55% to 65% when PF decreases from 0.3 to 0.0. The preshear contact friction shows the
 518 negligible influence on P_{sc} at a steady state. For Group C, compared with AR and PF , CP
 519 shows less influence on P_{sc} .

520 **5 Conclusion**

521 In this paper, a novel 3D SH-DEM approach has been developed for the simulation of 3D
 522 realistic irregular-shaped particles. In the 3D SH-DEM, the spherical harmonic transformation
 523 is first employed to represent particle shape in the local spherical coordination system. Then,
 524 using the SH-based particle model, the intrinsic physical properties can be easily computed.
 525 The novel numerical algorithms for identification of particle overlapping and contact
 526 resolutions are developed based on the spherical harmonic function and the node-to-surface
 527 scheme. The innovative features of the computational algorithms in the proposed 3D SH-DEM

528 are summarized as follows:

529 (a) The overlapping detection between SH-based irregular-shaped particles is implemented by
530 conventional global overlapping detection and unique local overlapping detection.
531 Conventional global overlapping detection is conducted by the combination of AABBs and the
532 spatial bins algorithm. The unique local overlapping detection is accomplished by (1)
533 discretizing the master particle into surface vertices, (2) substituting the discretized surface
534 vertices into the local spherical coordinate of slave particle, and (3) determining the penetration
535 condition of discretized surface vertices based on the spherical harmonic function of the slave
536 particle.

537 (b) The contact points are defined as the midpoints of the penetration vertices on the master
538 particle surface and the corresponding vertices on the slave particle surface with the same polar
539 angle at the local spherical coordinate system of the slave particle. The contact normal vector
540 at each contact is determined by the combination of the surface normal vectors of both the
541 master penetration vertices and corresponding vertices on the slave particle, which can be easily
542 and accurately computed based on the spherical harmonic functions.

543 (c) To determine the contact stiffness, the overlapping volume at each contact is computed based
544 on the local polyhedra, which are formed by the target penetration vertex and its one-ring
545 neighboring vertices.

546 Using the developed approach, three numerical examples were conducted to illustrate its
547 feasibility and capability. The simulation results are summarized as follows:

548 (a) Through simulations of the random deposition of superellipsoids with various shapes, the
549 evolutions of packing densities versus particle shapes are investigated and found to be
550 qualitatively consistent with the existing literature. The numerical results indicate that the
551 present SH-DEM model is reasonable for the simulation of non-spherical particles.

552 (b) Through simulating repose angle tests of realistic rock aggregates, it is indicated that the
553 contact friction coefficient between rocks should be taken as around 0.3 to simulate the realistic
554 repose angle of rocks in SH-DEM. Besides, the shape effects on macro- and micromechanical
555 properties of rock aggregate assemblies are primarily investigated through numerical repose
556 angle tests of spheres ($AR=1.0$), ellipsoids ($AR=0.6$), and realistic rock aggregates ($AR=0.6$)
557 using the SH-DEM. The shape effects on the angles of repose, mean coordination numbers, and
558 rotational motions are presented and compared.

559 (c) Through triaxial tests on rock aggregate assemblies, the effects of preshear contact friction,
560 particle aspect ratio, and confining pressure on the macroscopic and microscopic properties of
561 rock aggregates are presented. The simulation results of repose angle tests and triaxial tests
562 demonstrate that the developed SH-DEM approach is useful to investigate the shape effects on
563 the mechanical behaviors of realistic granular materials.

564 Indeed, compared with the simplified shape models such as disk-clump, the proposed method
565 can consider more realistic contact mechanics between irregular shape particles. The capability
566 and efficiency of the proposed SH-DEM program will pave a viable pathway for the researchers
567 to conduct more quantitative and credible studies on how the realistic particle shapes would

affect the macro- and micro-mechanical properties of granular materials. The method will be further be developed to incorporate more advanced computational algorithms, e.g., the effective energy-conserving contact modelling strategy [55], as future work.

Acknowledgments

The authors acknowledge the financial support provided by the National Natural Science Foundation of China under Grant No. 51938008 and No. 51878416.

References

- [1] Su, D., & Yan, W. M. 2018. 3D characterization of general-shape sand particles using microfocus X-ray computed tomography and spherical harmonic functions, and particle regeneration using multivariate random vector. *Powder Technology*, 323, 8-23.
- [2] Garboczi, E. J., & Bullard, J. W. 2013. Contact function, uniform-thickness shell volume, and convexity measure for 3d star-shaped random particles. *Powder Technology*, 237, 191–201.
- [3] Su, D., Wang, X., Yang, H., & Hong, C. Y. 2019. Roughness analysis of general-shape particles, from 2D closed outlines to 3D closed surfaces. *Powder Technology*. 356, 423-438
- [4] Cho, G. C., Dodds, J., & Santamarina, J. C. 2006. Particle shape effects on packing density, stiffness, and strength: natural and crushed sands. *Journal of geotechnical and geoenvironmental engineering*, 132(5), 591-602.
- [5] Nie, Z.H., Liang, Z.Y., & Wang, X. 2018. A three-dimensional particle roundness evaluation method. *Granular matter*. 20:31.

- 589 [6] Zhigang, Zhu, Huisu, Chen, Wenxiang, & Xu, et al. (2014). Parking simulation of three-
590 dimensional multi-sized star-shaped particles. *Modelling and Simulation in Materials Science and*
591 *Engineering*, 22(3), 35008-35008.
- 592 [7] Ting, J. M., Meachum, L., & Rowell, J. D. 1995. Effect of particle shape on the strength and
593 deformation mechanisms of ellipse-shaped granular assemblages. *Engineering Computations*,
594 12(2), 99-108.
- 595 [8] Lin, X., & Ng, T. T. 1995. Contact detection algorithms for three-dimensional ellipsoids in discrete
596 element modelling. *International Journal for Numerical and Analytical Methods in Geomechanics*,
597 19(9), 653-659.
- 598 [9] Lin, X., & Ng, T. T. 1997. A three-dimensional discrete element model using arrays of ellipsoids.
599 *Geotechnique*, 47(2), 319-329.
- 600 [10] Azéma, E., & Radjai, F. 2010. Stress-strain behavior and geometrical properties of packings of
601 elongated particles. *Physical Review E*, 81(5), 051304.
- 602 [11] Azéma, E., & Radjai, F. 2012. Force chains and contact network topology in sheared packings of
603 elongated particles. *Physical review E*, 85(3), 031303.
- 604 [12] Lu, P., Li, S., Zhao, J., & Meng, L. 2010. A computational investigation on random packings of
605 sphere-spherocylinder mixtures. *Science China Physics, Mechanics and Astronomy*, 53(12), 2284-
606 2292.
- 607 [13] Zhao, S., Zhang, N., Zhou, X., & Zhang, L. 2017. Particle shape effects on fabric of granular
608 random packing. *Powder technology*, 310, 175-186.
- 609 [14] Han, K., Feng, Y. T., & Owen, D. R. J. 2006. Polygon-based contact resolution for superquadrics.
610 *International journal for numerical methods in engineering*, 66(3), 485-501.
- 611 [15] Zhou, W., Huang, Y., Ng, T. T., & Ma, G. 2018. A geometric potential-based contact detection
612 algorithm for egg-shaped particles in discrete element modeling. *Powder Technology*, 327, 152-
613 162.

614 [16] Munjiza, A., Peters, J. F., Hopkins, M. A., Kala, R., & Wahl, R. E. 2009. A poly-ellipsoid particle
615 for non-spherical discrete element method. *Engineering Computations*.

616 [17] Zhao, S., & Zhao, J. 2019. A poly-superellipsoid-based approach on particle morphology for DEM
617 modeling of granular media. *International Journal for Numerical and Analytical Methods in*
618 *Geomechanics*, 43(13), 2147-2169.

619 [18] Feng, Y. T., & Owen, D. R. J. 2004. A 2D polygon/polygon contact model: algorithmic aspects.
620 *Engineering Computations*.

621 [19] Feng, Y.T., Tan, Y.Q., 2019. On Minkowski difference-based contact detection in
622 discrete/discontinuous modelling of convex polygons/polyhedra. *Engineering Computations*, 37(1),
623 54-72.

624 [20] Zhao, S., Zhao, J. 2020. SudoDEM : unleashing the predictive power of the discrete element method
625 on simulation for non-spherical granular particles. *Computer Physics Communications*.

626 [21] Ferrellec, J. F., & McDowell, G. R. 2008. A simple method to create complex particle shapes for
627 DEM. *Geomechanics and Geoengineering: An International Journal*, 3(3), 211-216.

628 [22] Zheng, J., & Hryciw, R. D. 2017. An image based clump library for DEM simulations. *Granular*
629 *Matter*, 19(2), 26.

630 [23] Yan, W. M. 2010. Particle elongation and deposition effect to macroscopic and microscopic
631 responses of numerical direct shear tests. *Geotechnical Testing Journal*, 34(3), 238-249.

632 [24] Nie, Z., Zhu, Y., Wang, X., & Gong, J. 2019. Investigating the effects of Fourier-based particle
633 shape on the shear behaviors of rockfill material via DEM. *Granular Matter*, 21(2), 22.

634 [25] Kodam, M., Bharadwaj, R., Curtis, J., Hancock, B., & Wassgren, C. 2009. Force model
635 considerations for glued-sphere discrete element method simulations. *Chemical Engineering*
636 *Science*, 64(15), 3466-3475.

637 [26] Höhner, D., Wirtz, S., Kruggel-Emden, H., & Scherer, V. 2011. Comparison of the multi-sphere
638 and polyhedral approach to simulate non-spherical particles within the discrete element method:
639 Influence on temporal force evolution for multiple contacts. *Powder Technology*, 208(3), 643-656.

640 [27] Li, Z.F. 2017. Validations and applications of discrete element method. The Hong Kong University
641 of Science and Technology: Hong Kong.

642 [28] Andrade, J. E., Lim, K. W., Avila, C. F., & Vlahinić, I. 2012. Granular element method for
643 computational particle mechanics. *Computer Methods in Applied Mechanics and Engineering*, 241,
644 262-274.

645 [29] Liu, S., Chen, F., Ge, W., & Ricoux, P. 2020. NURBS-based DEM for non-spherical particles.
646 *Particuology*, 49, 65-76.

647 [30] Kawamoto, R., Andò, E., Viggiani, G., & Andrade, J. E. 2018. All you need is shape: Predicting
648 shear banding in sand with LS-DEM. *Journal of the Mechanics and Physics of Solids*, 111, 375-
649 392.

650 [31] Lai, Z., Chen, Q., & Huang, L. 2020. Fourier series-based discrete element method for
651 computational mechanics of irregular-shaped particles. *Computer Methods in Applied Mechanics*
652 *and Engineering*, 362, 112873.

653 [32] Feng, Y.T., Han, K., Owen, D.R.J. Energy-conserving contact interaction models for arbitrarily
654 shaped discrete elements. *Computer Methods in Applied Mechanics & Engineering*, 2012. 205-208:
655 169-177.

656 [33] Feng, Y. T. An energy-conserving contact theory for discrete element modelling of arbitrarily
657 shaped particles: basic framework and general contact model. *Computer Methods in Applied*
658 *Mechanics and Engineering*, 2021, 373, 113454.

659 [34] Feng, Y.T. An energy-conserving contact theory for discrete element modelling of arbitrarily
660 shaped particles: Contact volume based model and computational issues. *Computer Methods in*
661 *Applied Mechanics and Engineering*, 2021. 373, 113493.

662 [35] Farsi, A., Xiang, J., Latham, J. P., Carlsson, M., & Marigo, M. 2020. Packing simulations of
663 complex-shaped rigid particles using FDEM: an application to catalyst pellets. *Powder Technology*,
664 380(8).

665 [36] Joulin, C., Xiang, J., Latham, J. P., Pain, C., Salinas, P. 2020. Capturing heat transfer for complex-
666 shaped multibody contact problems, a new FDEM approach. *Computational Particle Mechanics*,
667 7(5), 919-934.

668 [37] Latham, J.P., Xiang, J., Farsi, A., Joulin, C., & Karantzoulis, N. 2019. A class of particulate
669 problems suited to FDEM requiring accurate simulation of shape effects in packed granular
670 structures. *Computational Particle Mechanics*, 1-12.

671 [38] Munjiza, A., Rougier, E., Zhou, L., & Knight, E. E. 2020. FSIS: a novel fluid–solid interaction
672 solver for fracturing and fragmenting solids. *Computational Particle Mechanics*, 7(4).

673 [39] Thornton, C. 1992. Applications of DEM to process engineering problems. *Engineering*
674 *Computations*, 9(2), 289-297.

675 [40] Xiang, J., Munjiza, A., Latham, J.P., Guises, R. 2009. On the validation of DEM and FEM/DEM
676 models in 2D and 3D. *Engineering Computations*, 26(6), 673-687.

677 [41] Latham, J.P., Munjiza, A. 2004. The modelling of particle systems with real shapes. *Philosophical*
678 *Transactions: Mathematical, Physical and Engineering Sciences*, 362(1822), 1953-1972.

679 [42] Laursen, T., 2002. *Computational Contact and Impact Mechanics: Fundamentals of Modeling*
680 *Interfacial Phenomena in Nonlinear Finite Element Analysis*. Springer, Berlin.

681 [43] Puso, M. A., & Laursen, T. A. 2002. A 3D contact smoothing method using Gregory patches.
682 *International Journal for Numerical Methods in Engineering*, 54(8), 1161-1194.

683 [44] Lim, K.-W., Krabbenhoft, K., Andrade, J., 2014. On the contact treatment of non-convex particles
684 in the granular element method. *Computational Particle Mechanics*. 1 (3), 257–275.

685 [45] Zhao, S., Zhou, X., & Liu, W. 2015. Discrete element simulations of direct shear tests with particle
686 angularity effect. *Granular Matter*, 17(6), 793-806.

687 [46] Donev, A., Cisse, I., Sachs, D., Variano, E. A., Stillinger, F. H., Connelly, R., & Chaikin, P. M.
688 2004. Improving the density of jammed disordered packings using ellipsoids. *Science*, 303(5660),
689 990-993.

- [47] Zhou, Z. Y., Zou, R. P., Pinson, D., & Yu, A. B. 2011. Dynamic simulation of the packing of ellipsoidal particles. *Industrial & engineering chemistry research*, 50(16), 9787-9798.
- [48] Jiao, Y., Stillinger, F. H., & Torquato, S. 2009. Optimal packings of superballs. *Physical Review E*, 79(4), 041309.
- [49] Delaney, G. W., & Cleary, P. W. 2010. The packing properties of superellipsoids. *EPL (Europhysics Letters)*, 89(3), 34002.
- [50] Williams, J.R., Pentland, A.P. 1992. Superquadrics and modal dynamics for discrete elements in interactive design. *Engineering Computations*, 9(2), 115-127.
- [51] Owen, D. R. J. 2004. A Robust Contact Model for Rigid Super-Quadrics. In *Abstracts of the Papers Presented at the Regular Sessions of the Sixth World Congress on Computational Mechanics in Conjunction with the Second Asian-Pacific Congress on Computational Mechanics II*.
- [52] Munjiza, A., And, D., & Crook, A. 1998. An $M(M^{-1}K)^m$ proportional damping in explicit integration of dynamic structural systems. *International Journal for Numerical Methods in Engineering*, 41, 1277–1296.
- [53] Munjiza, A. 2004. *The combined finite-discrete element method*. John Wiley & Sons.
- [54] Munjiza, A. Latham, J.P., & John, N. 2003. 3D dynamics of discrete element systems comprising irregular discrete elements—integration solution for finite rotations in 3D. *International Journal for Numerical Methods in Engineering*, 56(1).
- [55] Feng, Y.T. An effective energy-conserving contact modelling strategy for spherical harmonic particles represented by surface triangular meshes with automatic simplification. *Comput. Methods Appl. Mech. Engrg.* 2021, 379: 113750.

Tables

Table 1 DEM simulation parameters

Parameter	Value
Particle density, ρ (kg/m ³)	2700
Damping coefficient, α	0.3
Volumetric normal contact stiffness, k_n (N/m ³)	1×10^{11}
Shear contact stiffness, k_t (N/m)	1×10^7
Contact friction	0.48

718 **Appendix A Motion of particles in SH-DEM**

719 In the proposed SH-DEM, for each particle, the motion can be divided into two parts: translation
720 in the global coordinate system and rotation in the local coordinate system. To facilitate
721 numerical processing, the global coordinate system is usually the world coordinate system of
722 the particle system, while the local coordinate system is fixed on the individual particle and
723 moves synchronously with the particle.

724 The translational motion of a particle in the global coordinate system is governed by Newton
725 equations:

$$m \frac{d\mathbf{v}_i}{dt} = \mathbf{F}_i \quad (\text{A1})$$

726 where m is the particle mass; \mathbf{v}_i is the translational velocity along the i axis of the global
727 coordinate system; $i \in \{1,2,3\}$ represents the axis of the global coordinate system, and \mathbf{F}_i is
728 the total resultant force acting on the particle centroid (mass center), which can be calculated
729 as:

$$\mathbf{F}_i = \sum_{k=1}^{N_c} \mathbf{F}_k^c + \mathbf{F}^b + \mathbf{F}^d \quad (\text{A2})$$

730 where N_c is the contact number of the particle; \mathbf{F}^b is the body force, e.g., gravitational force;
731 \mathbf{F}^d is the damping force; and \mathbf{F}_k^c is the contact force acting at the k_{th} contact.

732 Compared with the contact force between the spherical particles, a remarkable feature of the
733 contact force between irregular-shaped particles is that the normal component of the contact
734 force (normal contact force) usually does not pass through the particle's center of mass, so the
735 torque around the center of mass can be generated. The torque can promote or inhibit the
736 rotation of the irregular-shaped particle. In a local coordinate system, Euler's equations are
737 applied to particle rotations:

$$I_i \frac{d\omega_i}{dt} - (I_j - I_k)\omega_j\omega_k = M_i \quad (\text{A3})$$

738 where $i, j, k \in 1, 2, 3$ is the principal axis; I_i is the principal moment of inertia; ω_i is the
 739 angular velocity, and M_i is the i_{th} component of the total resultant torque M , which can be
 740 calculated as:

$$M = \sum_{k=1}^{N_c} \mathbf{F}_k^c \times \mathbf{r}_k + M^d \quad (\text{A4})$$

741 where \mathbf{r}_k is the radical vector of the k_{th} contact; and M^d is the damping moment.

742 To stabilize the system after a reasonable number of iterations, following general DEM codes,
 743 artificial numerical damping is used to dissipate the kinetic energy. In this study, two types of
 744 damping are facilitated: local damping and viscous damping. Local damping provides damping
 745 to reduce the particle speed through adjustment of the resultant external force. Note that the
 746 resultant force discussed here includes the resultant force moment, and the velocity includes
 747 the angular velocity of rotation. Generally, a fixed coefficient, i.e., the damping coefficient, is
 748 used to adjust the resultant external forces and a corresponding damping force F_i^d is added to
 749 the right-hand side of the Newton equation and Euler's equations, given as:

$$F_i^d = -\alpha F_i \text{Sign} \left(F_i \left(v_i^{(t-\Delta t/2)} + \frac{dv_i^t}{dt} \frac{\Delta t}{2} \right) \right) \quad (\text{A5})$$

$$M_i^d = -\alpha M_i \text{Sign} \left(M_i \left(\omega_i^{(t-\Delta t/2)} + \frac{d\omega_i^t}{dt} \frac{\Delta t}{2} \right) \right)$$

750 where α is the damping coefficient; Δt is the time step; $v_i^{(t-\Delta t/2)}$ and $\omega_i^{(t-\Delta t/2)}$ are the
 751 previous mid-step translational velocity and angular velocity, respectively; $\frac{dv_i^t}{dt}$ and $\frac{d\omega_i^t}{dt}$ are
 752 the current on-step translational acceleration and angular acceleration, respectively; and
 753 $\text{Sign}(x)$ is the signum function:

$$\text{Sign}(x) = \begin{cases} -1 & \text{if } x < 0, \\ 0 & \text{if } x = 0, \\ 1 & \text{if } x > 0. \end{cases} \quad (\text{A6})$$

Viscous damping is a kind of damping applied at the contact of particles, which can reduce the relative velocity of two contact particles by adjusting the contact force. The normal and tangential viscous damping forces F_n^d and F_t^d are calculated by:

$$\begin{aligned} F_n^d &= 2\sqrt{\bar{m}k_n}\beta_n V_n \\ F_t^d &= 2\sqrt{\bar{m}k_t}\beta_t V_t \end{aligned} \quad (\text{A7})$$

where $\bar{m} = m^M m^S / (m^M + m^S)$ is the equivalent mass of the two contacted particles; β_n and β_t are the normal and tangential viscous damping coefficients, respectively; and V_n and V_t are the normal and tangential components of the relative velocity of the two particles at the contact. It should be noted that the viscous damping force should not exceed the corresponding contact force. The Eq. (A7) is based on the previous work [45]. Similar approach can be referred to [52][53].

Appendix B Scheme of computation in SH-DEM

The computational iteration of the proposed SH-DEM includes two components: the particle system and the contact system. In the particle system, the change in the particle position is accompanied by the appearance or disappearance of interparticle contact. The computation scheme can be concluded as: (1) Given the position of particles in the system, determine the corresponding geometric information of the contact between particles through contact detection between particles; (2) According to the given contact model, calculate the contact force at each contact and the resulted moment acted on each particle; (3) Based on the given movement law (Newton's second law), calculate the motion of the particles and drive the particles to the new positions; (4) continue the next computation cycle from (1) to (3).

774 The so-called central difference method is done to solve the particle motion (Newton's and
 775 Euler's equations. A brief description of the solution process of Newton's equation based on the
 776 standard leapfrog algorithm is adopted.

777 (1) Given a specific position vector \mathbf{x}^t at time t and the position vector $\mathbf{x}^{t-\Delta t}$ at time $t -$
 778 Δt , calculate the translational velocity $\mathbf{v}^{t-\frac{\Delta t}{2}}$ at time $t - \frac{\Delta t}{2}$:

$$\mathbf{v}^{t-\frac{\Delta t}{2}} = \frac{\mathbf{x}^t - \mathbf{x}^{t-\Delta t}}{\Delta t} \quad (\text{B1})$$

779 (2) Calculate the translational acceleration \mathbf{a}^t at time t :

$$\mathbf{a}^t = \frac{\mathbf{F}}{m} \quad (\text{B2})$$

780 (3) Calculate the translational velocity $\mathbf{v}^{t+\frac{\Delta t}{2}}$ at time $t + \frac{\Delta t}{2}$:

$$\mathbf{v}^{t+\frac{\Delta t}{2}} = \mathbf{v}^{t-\frac{\Delta t}{2}} + \mathbf{a}^t \Delta t \quad (\text{B3})$$

781 (4) Calculate the position vector $\mathbf{x}^{t+\Delta t}$ at time $t + \Delta t$:

$$\mathbf{x}^{t+\Delta t} = \mathbf{x}^t + \mathbf{v}^{t+\frac{\Delta t}{2}} \Delta t \quad (\text{B4})$$

782 For Euler's equations, based on the previous development [54], the extending leapfrog
 783 algorithm is employed as follows:

784 (1) Given a specific angular momentum $L^{t-\frac{\Delta t}{2}}$ at time $t - \frac{\Delta t}{2}$ and external resultant moment
 785 M^t at time t , the angular momentum at time t and $t + \frac{\Delta t}{2}$ can be calculated as:

$$L^t = L^{t-\frac{\Delta t}{2}} + M^t \frac{\Delta t}{2} \quad (\text{B5})$$

$$L^{t+\frac{\Delta t}{2}} = L^{t-\frac{\Delta t}{2}} + M^t \Delta t \quad (\text{B6})$$

786 (2) The corresponding local angular velocity $\hat{\omega}^t$ at the local coordinate system can be
 787 calculated by:

$$\hat{\omega}^t = \mathbf{I}^{-1} \mathbf{T} L^t \quad (\text{B7})$$

$$\hat{\omega}^{t+\frac{\Delta t}{2}} = \mathbf{I}^{-1} \mathbf{T} \mathbf{L}^{t+\frac{\Delta t}{2}} \quad (\text{B8})$$

788 where \mathbf{T} is the rotation matrix transformed from global coordinates to local coordinates at time
 789 t , which can be obtained by the quaternion matrix q^t .

790 (3) The change rate of q^t with respect to time t , denoted as \dot{q}^t , can be calculated as:

$$\dot{q}^t = \begin{bmatrix} \dot{q}_\omega^t \\ \dot{q}_x^t \\ \dot{q}_y^t \\ \dot{q}_z^t \end{bmatrix} = \frac{1}{2} \begin{bmatrix} q_\omega^t & -q_x^t & -q_y^t & -q_z^t \\ q_x^t & q_\omega^t & -q_z^t & q_y^t \\ q_y^t & q_z^t & q_\omega^t & -q_x^t \\ q_z^t & -q_y^t & q_x^t & q_\omega^t \end{bmatrix} \begin{bmatrix} 0 \\ \hat{\omega}_x^t \\ \hat{\omega}_y^t \\ \hat{\omega}_z^t \end{bmatrix} \quad (\text{B9})$$

791 and the quaternion matrix $q^{t+\frac{\Delta t}{2}}$ can be calculated as:

$$q^{t+\frac{\Delta t}{2}} = q^t + \dot{q}^t \frac{\Delta t}{2} \quad (\text{B10})$$

792 (4) The global angular velocity $\omega^{t+\frac{\Delta t}{2}}$ at time $t + \frac{\Delta t}{2}$ can be calculated by:

$$\omega^{t+\frac{\Delta t}{2}} = \mathbf{T}^{-1} \hat{\omega}^{t+\frac{\Delta t}{2}} \quad (\text{B11})$$

793 The solution involves explicit finite difference with incremental time steps, which is dependent
 794 on the incremental time step Δt . On the one hand, in the particle system, the movement of a
 795 single particle at each time step needs to be small enough so that the movement of a single
 796 particle only affects the surrounding particles. On the other hand, when using the central
 797 difference method, the time step Δt needs to be small enough to keep the error in the particle
 798 motion solution as small as possible. Therefore, scholars have put forward the concept of the
 799 critical time step that the maximum time step should satisfy the numerical stability. However,
 800 due to the complexity of the particle system, there is no unified theoretical derivation for the
 801 determination of the critical time step. The smaller the time step is, the more accurate the
 802 particle motion calculation is, and the more stable the numerical value is. The very accurate
 803 calculation of the movement of each particle will not change (or improve) the simulation results
 804 substantially, but will significantly increase the calculation time, which is obviously of no

805 practical significance. Hence, to make simulation numerically stable, the present timestep in
806 this study will be tentatively selected based on empirical trials.

807

808 Figure captions

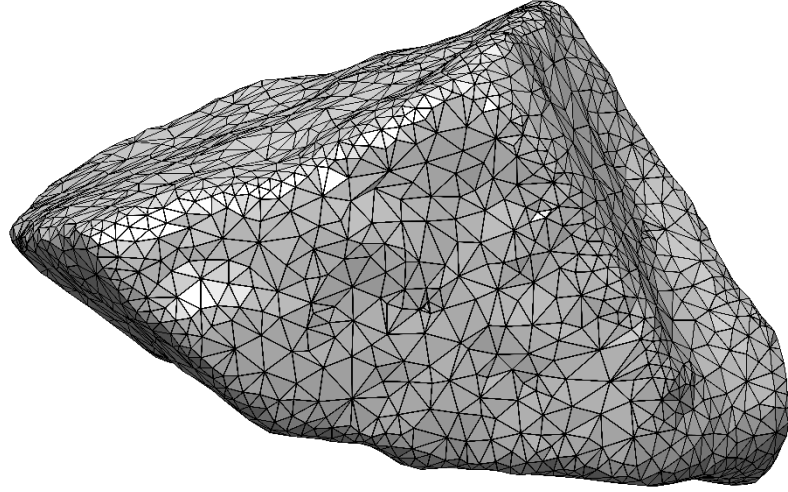
- 809 Fig. 1 The digitalized models of realistic rock particle: (a) triangular mesh model obtained from 3D
810 laser scanning, (b) transform discrete surface vertices from Cartesian Coordinate to Spherical
811 Coordinate, (c) continuously representation of the discrete particle surface using the spherical harmonic
812 function
- 813 Fig. 2 AABB of an example particle in the global Cartesian coordinate system
- 814 Fig. 3 determine the potential overlapping range of spherical angles: (a) Circumscribed spheres of MG
815 and SG, (b) Potential overlapping range
- 816 Fig. 4 Example of surface discretization with vertices in white seeded on the within the identified
817 potential overlapping region: (a) full-space view, (b) half-space view
- 818 Fig. 5 Location of $Q_i' [r_i^{M'}(\theta'_i, \varphi'_i)]$ of MG with respect to SG: (a) when MG vertex Q_i outside SG,
819 (b) when MG vertex Q_i inside SG, (a) when MG vertex Q_i on SG surface
- 820 Fig. 6 Definition of contact point C_i for a pair of penetration points Q_i and P_i
- 821 Fig. 7 Definition of contact normal vector \vec{n}_i at contact point C_i
- 822 Fig. 8 Definition of local overlapping volume V_i at contact point C_i : (a) whole particle view, (b) local
823 region view, (c) one-ring-neighbor vertices, (d) Example of $V_{P_i P_i^k P_i^{k+1} Q_i Q_i^k Q_i^{k+1}}$, (e) the local overlapping
824 volume V_i , (f) the top and base facets of V_i
- 825 Fig. 9 Packing of some example superellipsoid particles (a) $\eta=2.0$; (b) $\eta=1.25$; (c) $\eta=0.8$; (d) $\eta=0.5$;
826 (e) $\zeta=0.5$; (f) $\zeta=0.8$; (g) $\zeta=1.2$; (h) $\zeta=1.5$
- 827 Fig. 10 Packing density for superellipsoid (a) with different η and (b) with different ζ
- 828 Fig. 11 Mean coordination number Z for superellipsoid (a) with different η and (b) with different ζ
- 829 Fig. 12 Laboratory test of the angle of repose (a) container; (b) test step, (c) lift side-wall (d)
830 measurement of the repose angle
- 831 Fig. 13 Illustration of (a) the real crushed rock for testing and (b) the 3D virtual model obtained by the
832 3D laser scanner
- 833 Fig. 14 Numerical test of repose angle in SH-DEM: (a) Initial sample; (b) During testing
- 834 Fig. 15 Repose angles of samples with different contact friction coefficients: (a) contact friction = 0.1;
835 (b) contact friction = 0.2; (c) contact friction = 0.3; (d) contact friction = 0.5
- 836 Fig. 16 Ranges of shapes and the snapshots of example crushed rocks
- 837 Fig. 17 Repose angles of samples with different particle shapes: (a) spherical particle with AR=1.0;
838 (b) ellipsoid particle with AR=0.65; (c) crushed rocks with AR=0.65
- 839 Fig. 18 Evolution of mean coordination number during repose angle tests for different samples
- 840 Fig. 19 Evolution of mean rotational displacement during repose angle tests for different samples
- 841 Fig. 20 Ranges of shapes and the snapshots of example crushed rocks in Group C
- 842 Fig. 21 (a) non-overlapped rock aggregates; (b) consolidated rock aggregate sample; (c) Sheared rock
843 aggregate sample
- 844 Fig. 22 Comparison of deviatoric stress between (a) samples of different AR; (b) samples of different
845 preshear contact friction; (c) samples of different confining pressure
- 846 Fig. 23 Comparison of volumetric strain between (a) samples of different AR; (b) samples of different
847 preshear contact friction; (c) samples of different confining pressure

848 Fig. 24 Comparison of volumetric strain between (a) samples of different AR; (b) samples of different
849 preshear contact friction; (c) samples of different confining pressure

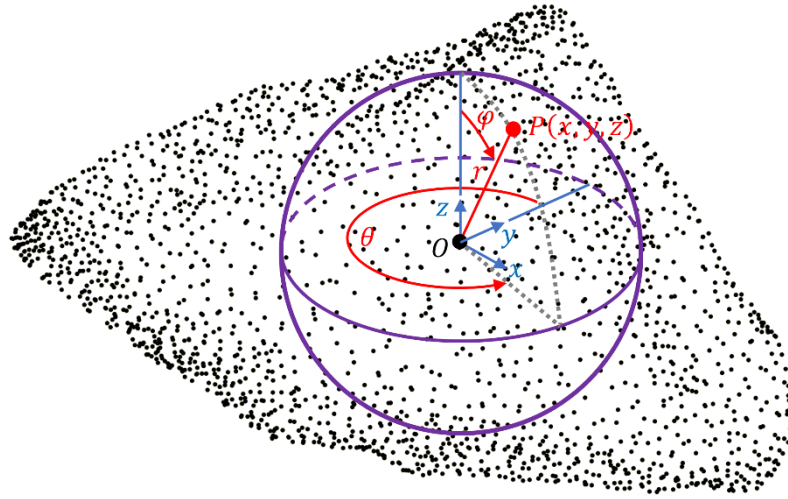
850 Fig. 25 Comparison of percentage of sliding contact between (a) samples of different AR; (b) samples
851 of different preshear contact friction; (c) samples of different confining pressure

852

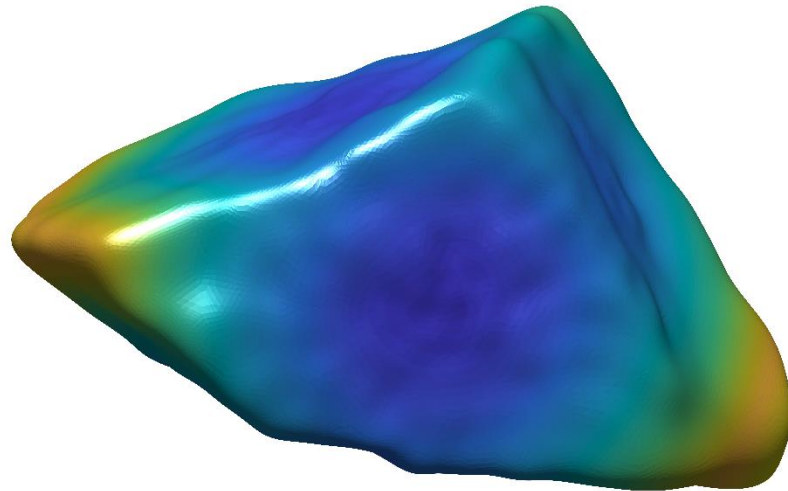
853



(a)



(b)



(c)

Fig. 1 The digitalized models of realistic rock particle: (a) triangular mesh model obtained from 3D laser scanning, (b) transform discrete surface vertices from Cartesian Coordinate to Spherical Coordinate, (c) continuously representation of the discrete particle surface using the spherical harmonic function

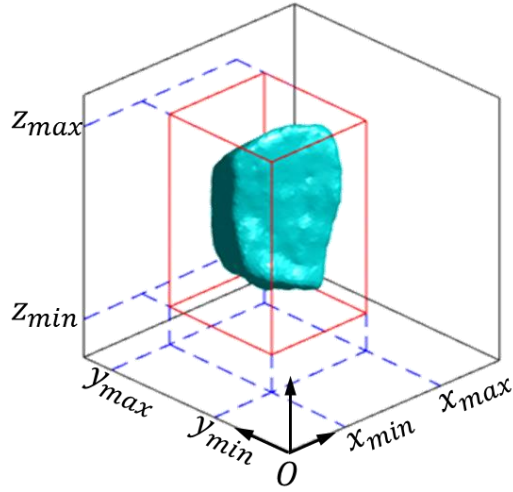


Fig. 2 AABB of an example particle in the global Cartesian coordinate system

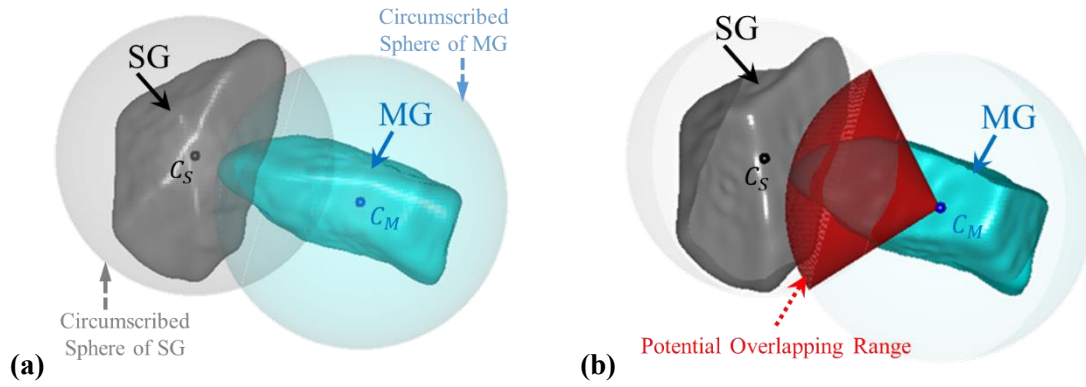


Fig. 3 determine the potential overlapping range of spherical angles: (a) Circumscribed spheres of MG and SG, (b) Potential overlapping range

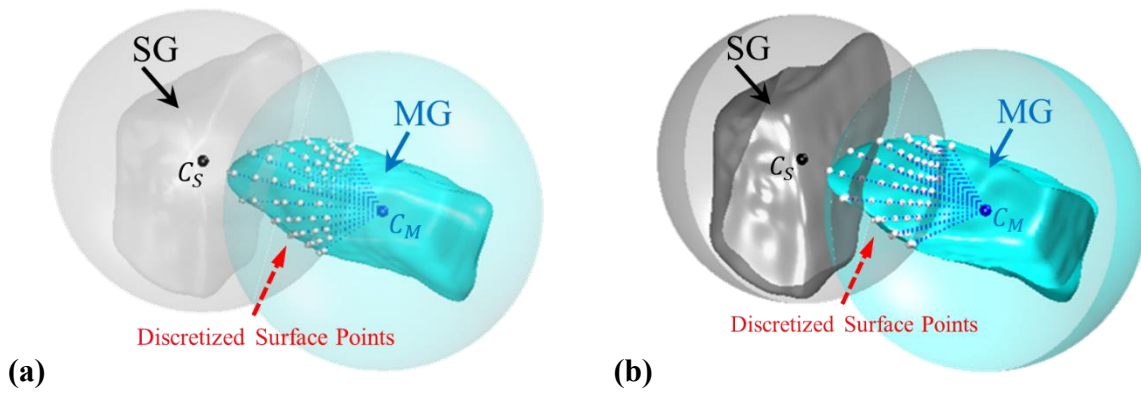
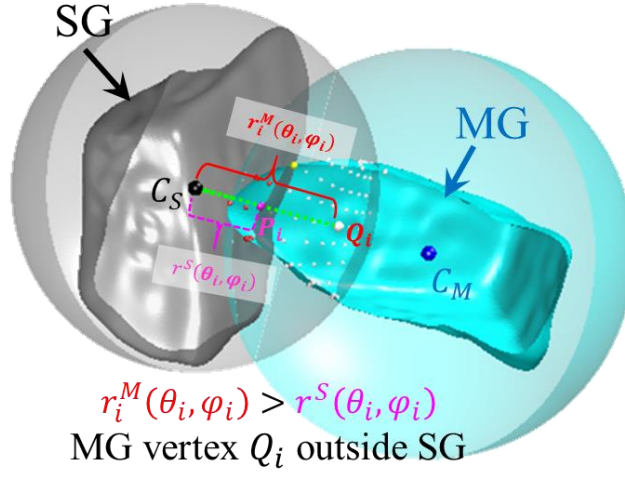
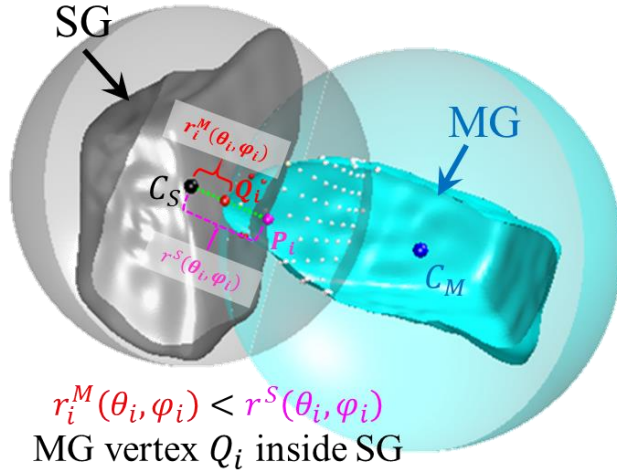


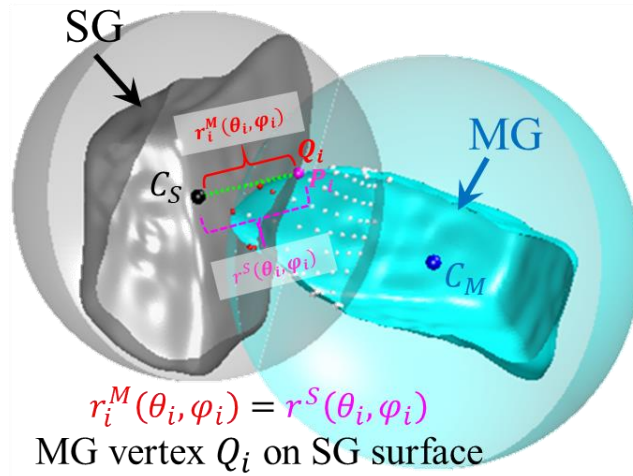
Fig. 4 Example of surface discretization with vertices in white seeded on the within the identified potential overlapping region: (a) full-space view, (b) half-space view



(a)



(b)



(c)

Fig. 5 Location of $Q_i[r_i^{M'}(\theta'_i, \varphi'_i)]$ of MG with respect to SG: (a) when MG vertex Q_i outside SG, (b) when MG vertex Q_i inside SG, (a) when MG vertex Q_i on SG surface

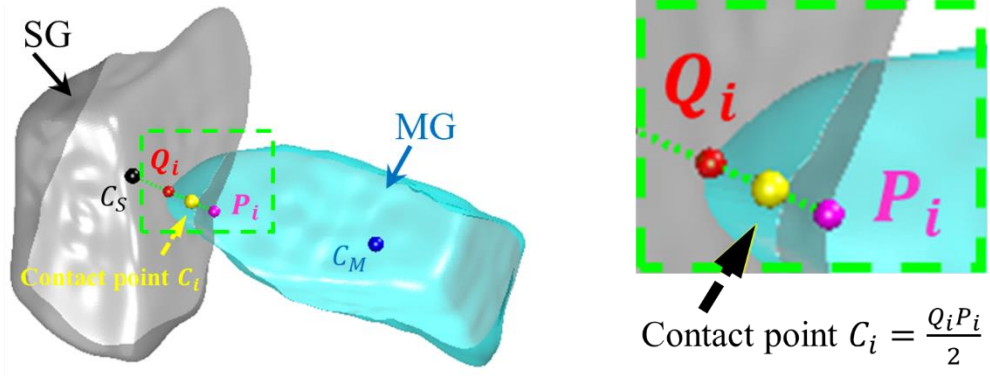


Fig. 6 Definition of contact point C_i for a pair of penetration points Q_i and P_i

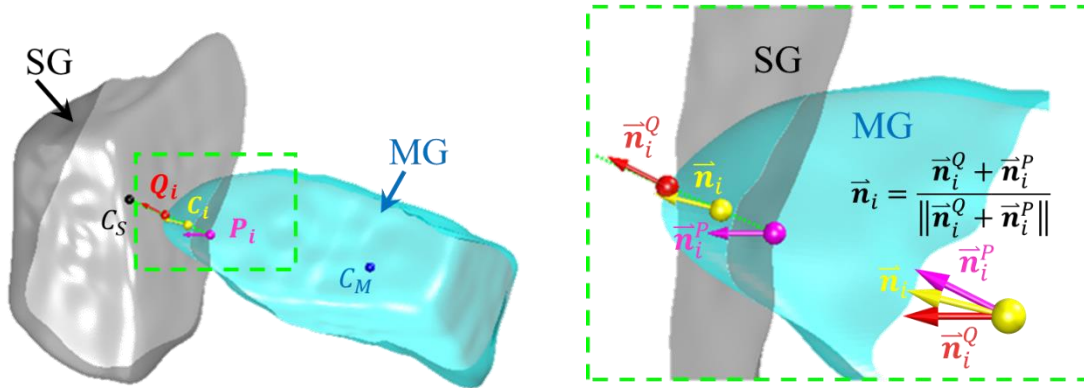


Fig. 7 Definition of contact normal vector \vec{n}_i at contact point C_i

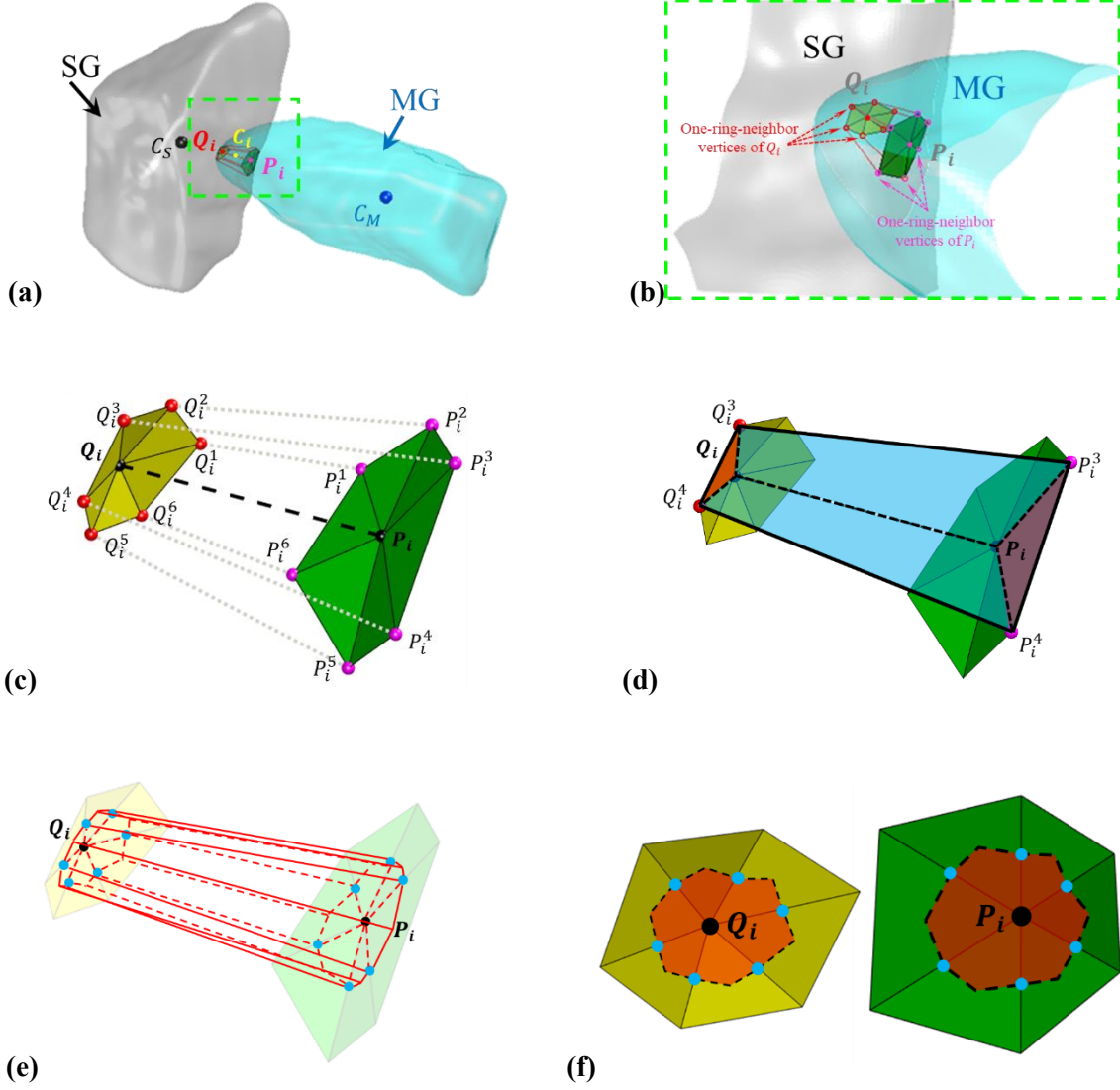


Fig. 8 Definition of local overlapping volume V_i at contact point C_i : (a) whole particle view, (b) local region view, (c) one-ring-neighbor vertices, (d) Example of $V_{P_i P_i^k P_i^{k+1} Q_i Q_i^k Q_i^{k+1}}$, (e) the local overlapping volume V_i , (f) the top and base facets of V_i

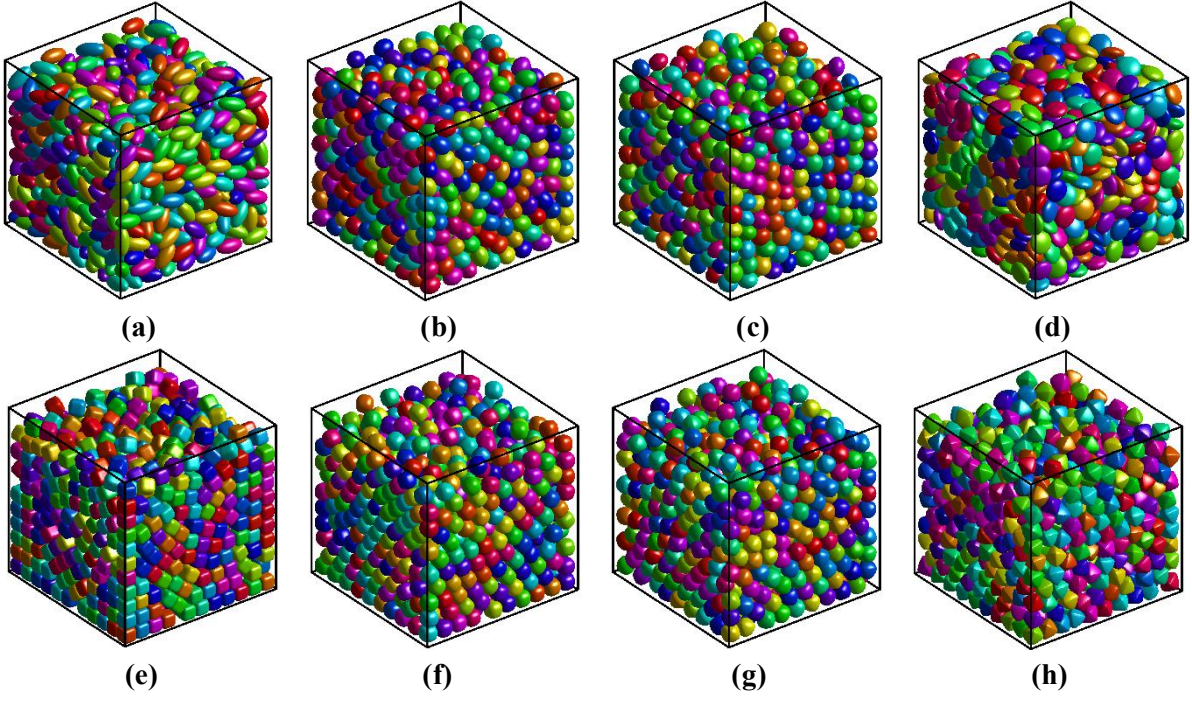
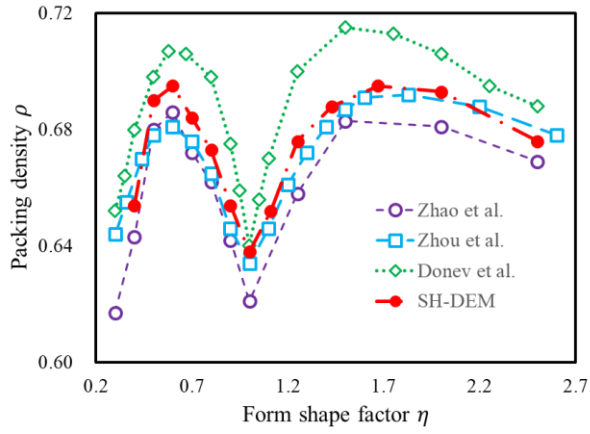
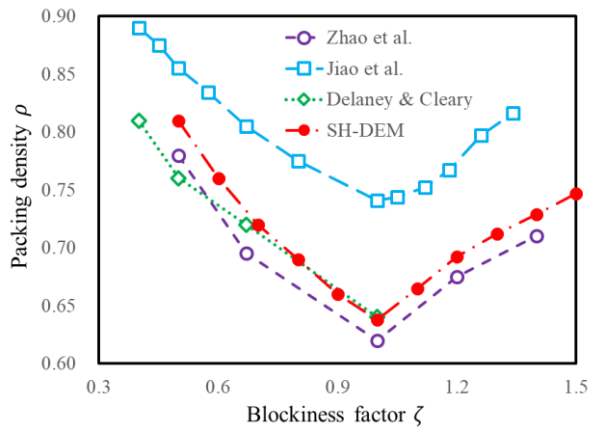


Fig. 9 Packing of some example superellipsoid particles (a) $\eta=2.0$; (b) $\eta=1.25$; (c) $\eta=0.8$; (d) $\eta=0.5$; (e) $\zeta=0.5$; (f) $\zeta=0.8$; (g) $\zeta=1.2$; (h) $\zeta=1.5$

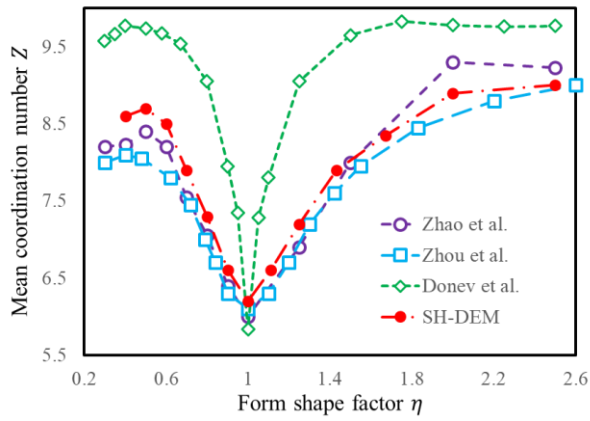


(a)

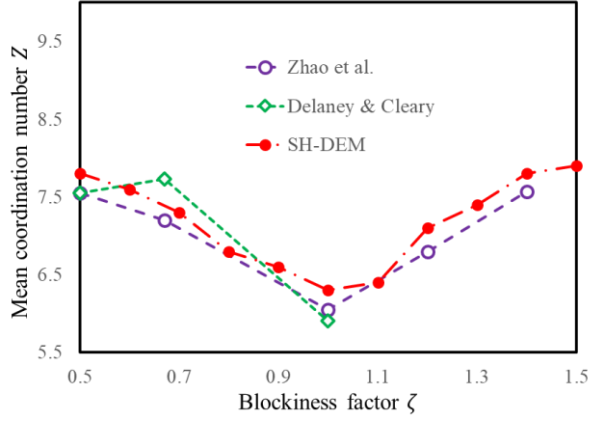


(b)

Fig. 10 Packing density for superellipsoid (a) with different η and (b) with different ζ



(a)



(b)

Fig. 11 Mean coordination number Z for superellipsoid (a) with different η and (b) with different ζ

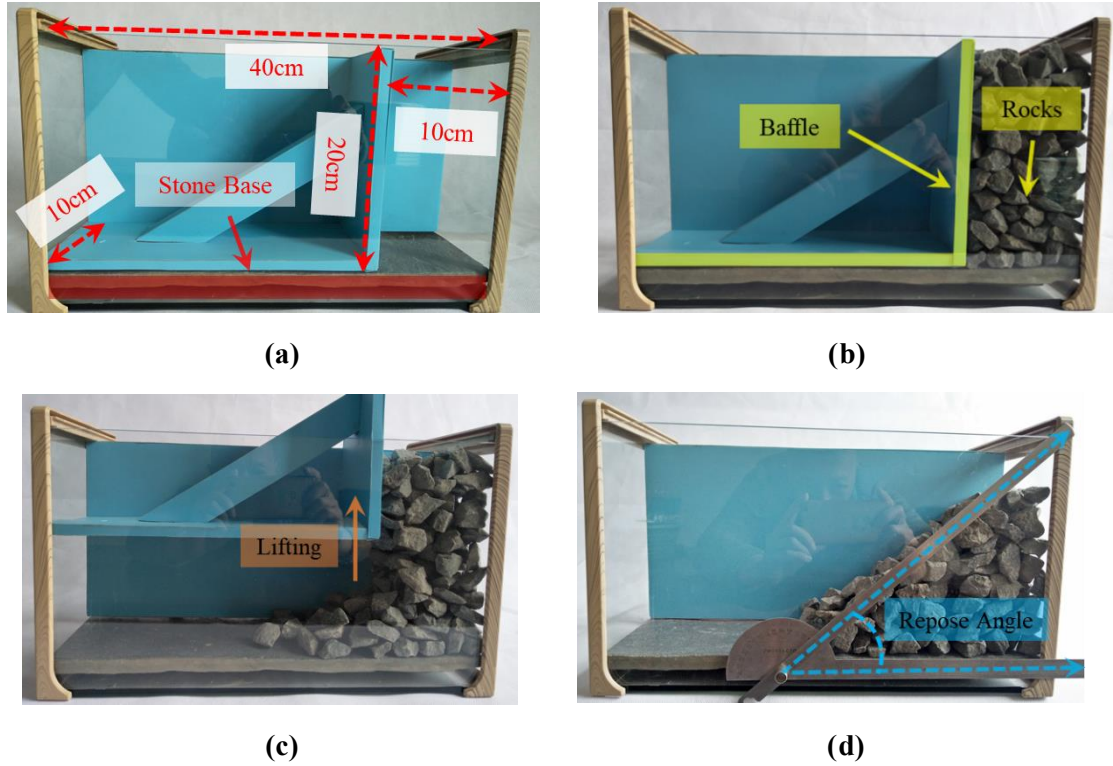


Fig. 12 Laboratory test of the angle of repose (a) container; (b) test step, (c) lift side-wall (d) measurement of the repose angle



Fig. 13 Illustration of (a) the real crushed rock for testing and (b) the 3D virtual model obtained by the 3D laser scanner

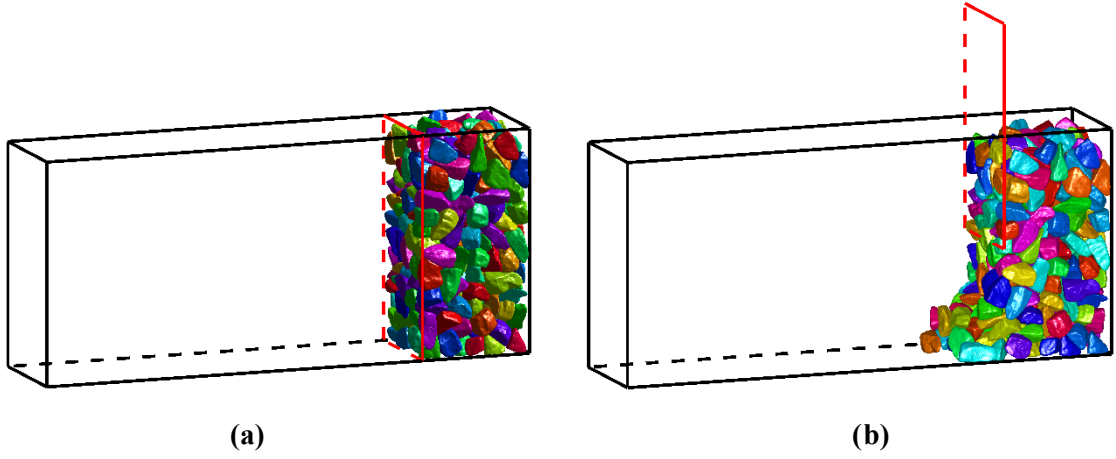


Fig. 14 Numerical test of repose angle in SH-DEM: (a) Initial sample; (b) During testing

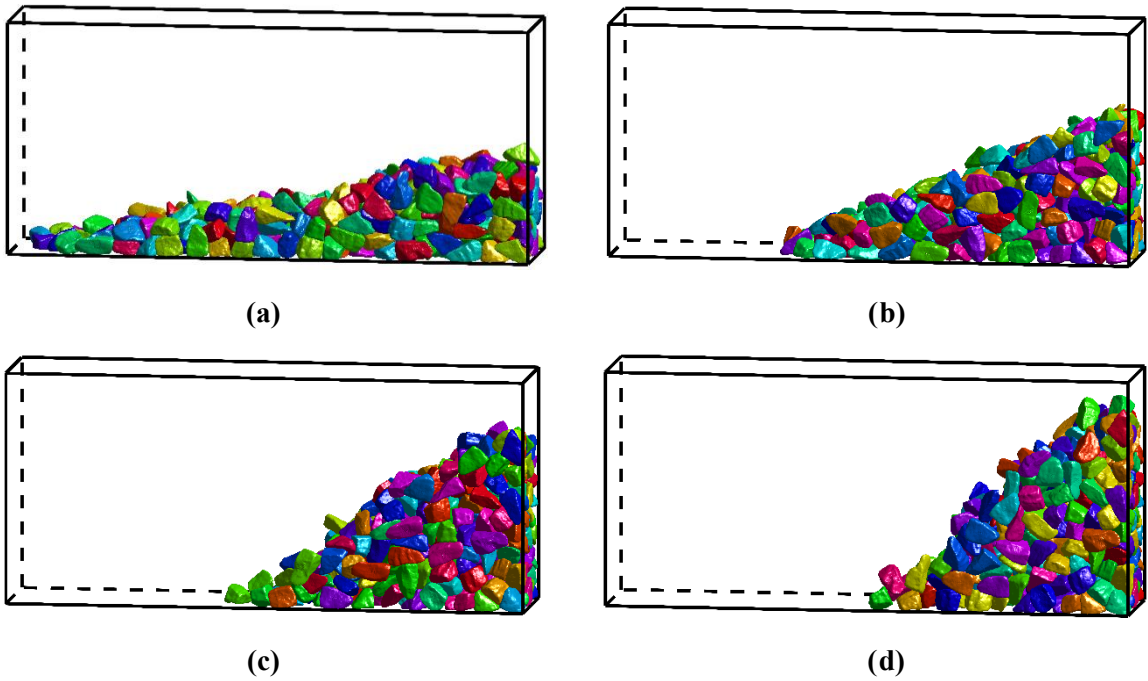


Fig. 15 Repose angles of samples with different contact friction coefficients: (a) contact friction = 0.1; (b) contact friction = 0.2; (c) contact friction = 0.3; (d) contact friction = 0.5

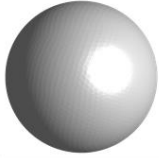
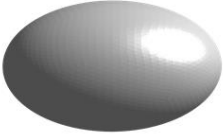
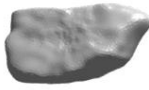
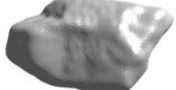
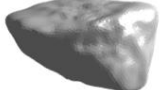
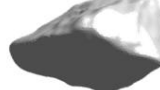
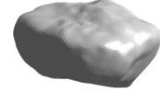
S1 – Sphere					
AR=1.0					
S2 – Ellipsoid					
AR=0.65					
S3 – Rocks					
AR=0.65					

Fig. 16 Ranges of shapes and the snapshots of example crushed rocks

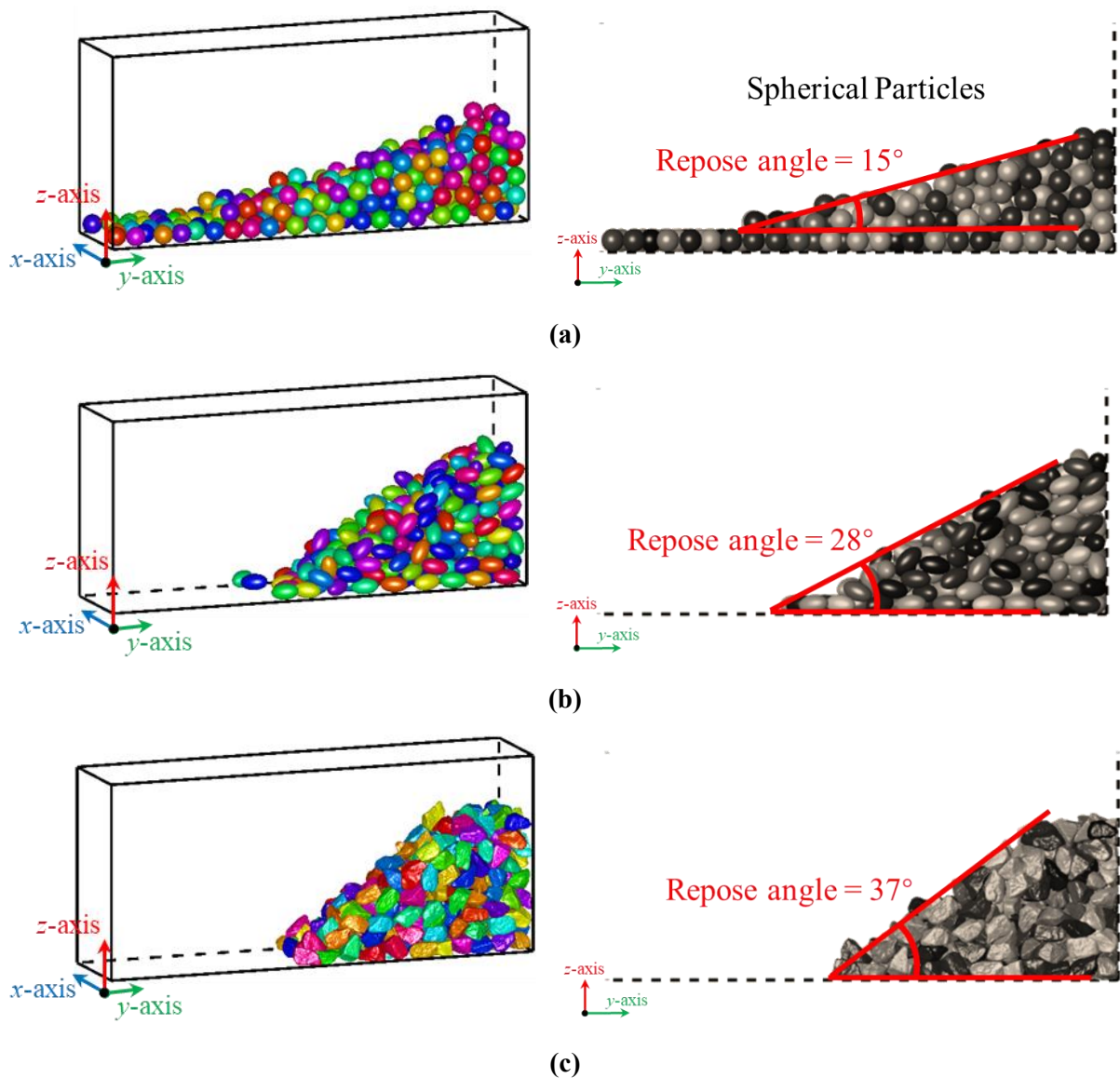


Fig. 17 Repose angles of samples with different particle shapes: (a) spherical particle with AR=1.0; (b) ellipsoid particle with AR=0.65; (c) crushed rocks with AR=0.65

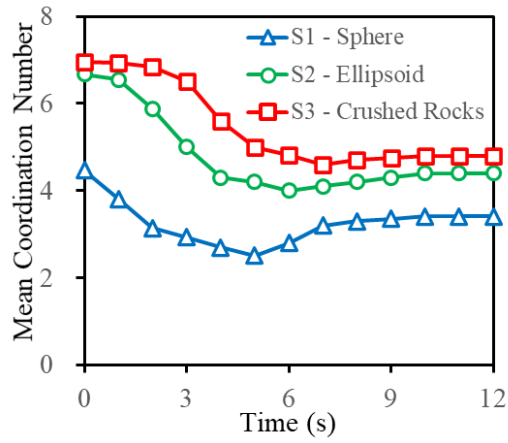


Fig. 18 Evolution of mean coordination number during repose angle tests for different samples

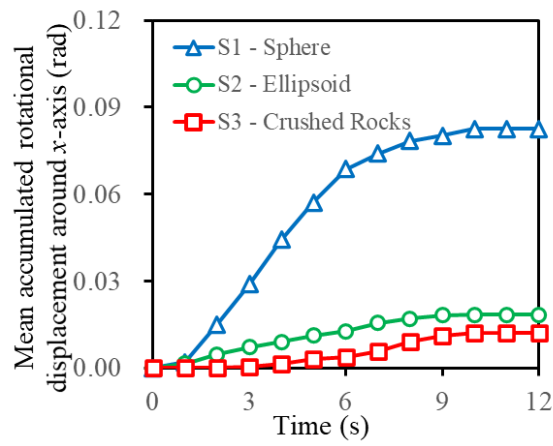


Fig. 19 Evolution of mean rotational displacement during repose angle tests for different samples

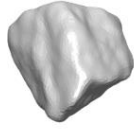
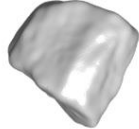
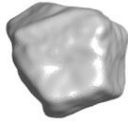
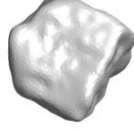
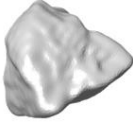
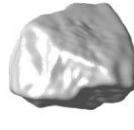
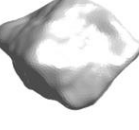
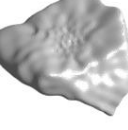
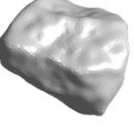
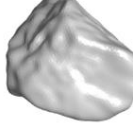
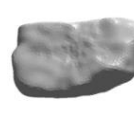
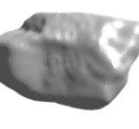
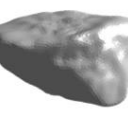
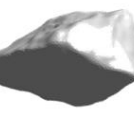
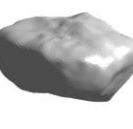
Sample 1					
AR=0.90~1.00					
Sample 2					
AR=0.75~0.85					
Sample 3					
AR=0.60~0.70					

Fig. 20 Ranges of shapes and the snapshots of example crushed rocks in Group C

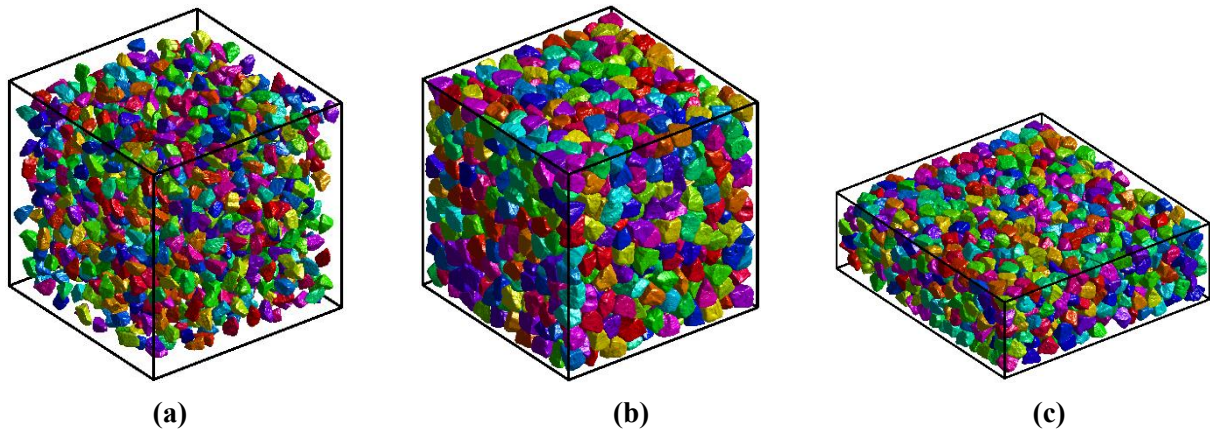


Fig. 21 (a) non-overlapped rock aggregates; (b) consolidated rock aggregate sample; (c) Sheared rock aggregate sample

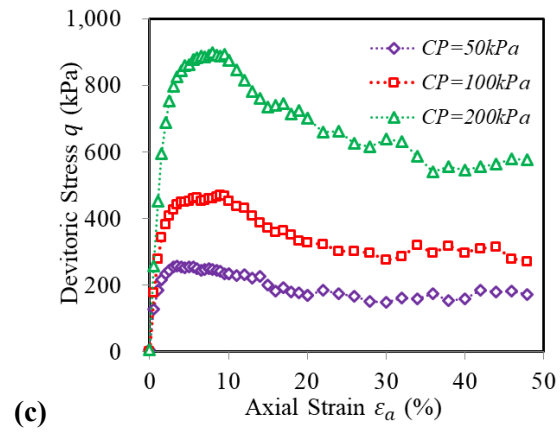
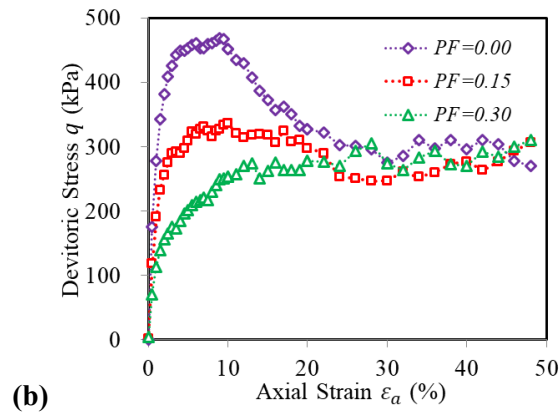
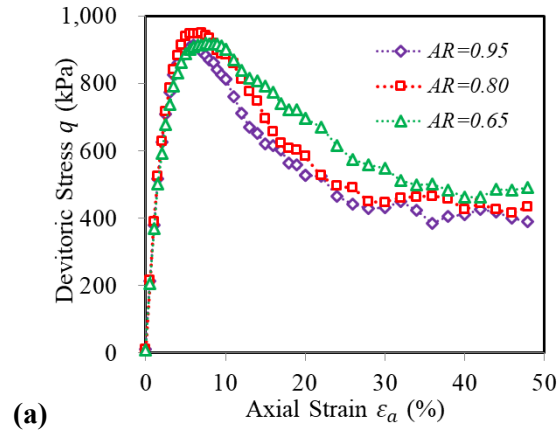


Fig. 22 Comparison of deviatoric stress between (a) samples of different AR; (b) samples of different preshear contact friction; (c) samples of different confining pressure

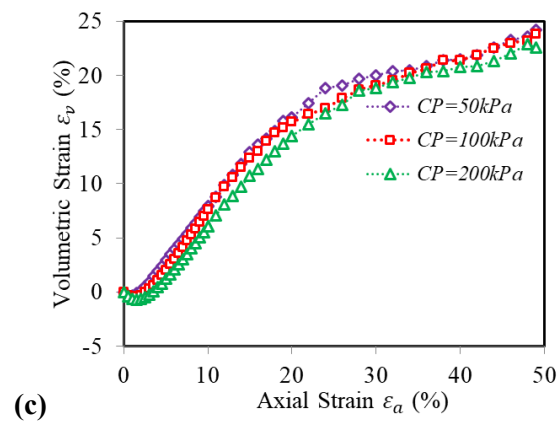
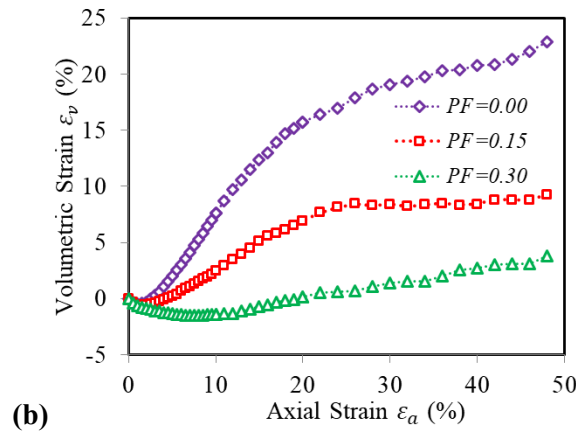
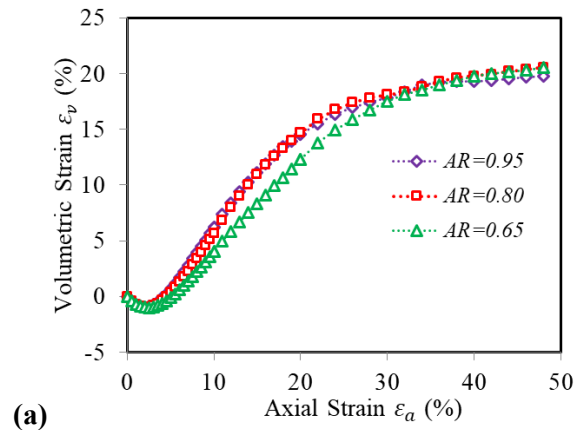
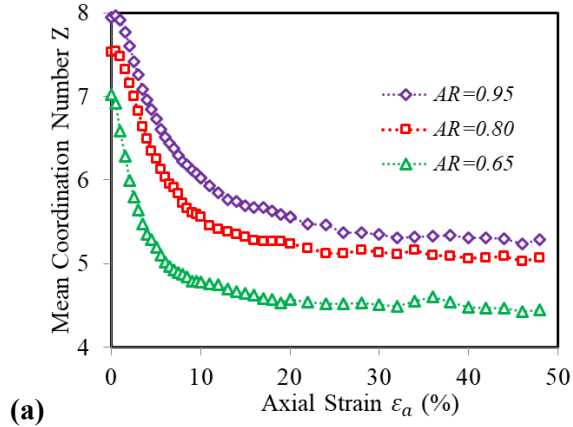
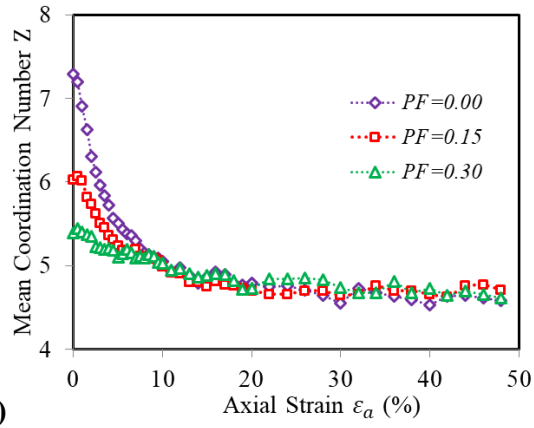


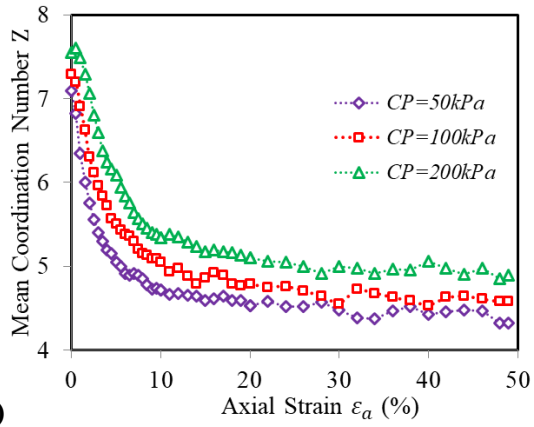
Fig. 23 Comparison of volumetric strain between (a) samples of different AR; (b) samples of different preshear contact friction; (c) samples of different confining pressure



(a)



(b)



(c)

Fig. 24 Comparison of volumetric strain between (a) samples of different AR; (b) samples of different preshear contact friction; (c) samples of different confining pressure

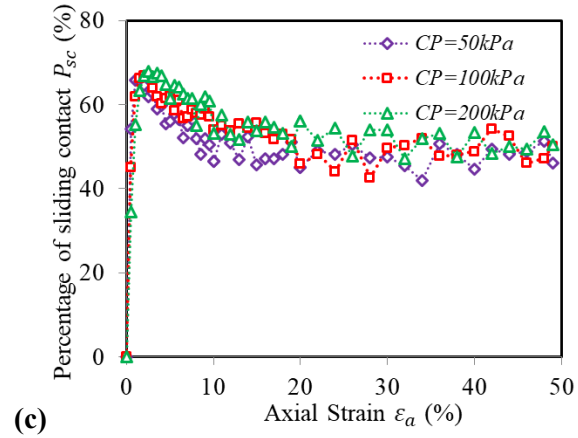
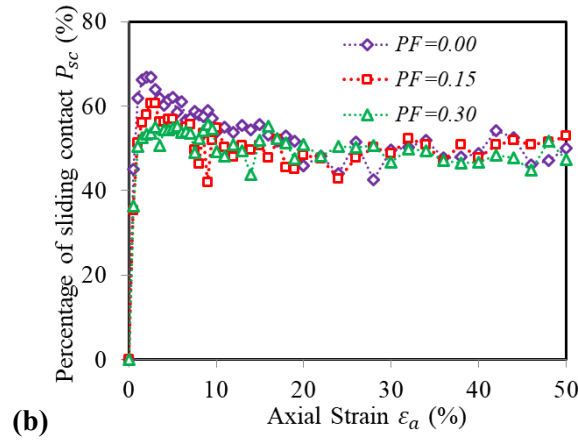
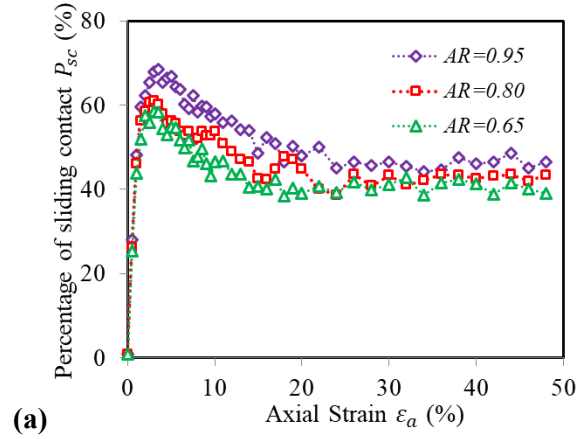


Fig. 25 Comparison of percentage of sliding contact between (a) samples of different AR; (b) samples of different preshear contact friction; (c) samples of different confining pressure